2007:221 CIV

MASTER'S THESIS

Sea Ice Monitoring in the Arctic Using Satellite SAR Images

Johan Wåhlin

Luleå University of Technology

MSc Programmes in Engineering
Space Engineering
Department of Applied Physics and Mechanical Engineering
Division of Physics

2007:221 CIV - ISSN: 1402-1617 - ISRN: LTU-EX--07/221--SE

Abstract

Synthetic Aperture Radar (SAR) with its high resolution and capability to see through clouds is suitable for studying sea ice, an important parameter for global climate but which due to its remoteness little is known about.

To study the motion of sea ice, manual drift vectors have been acquired from every three days from Envisat SAR wide swath image pairs with 150 m resolution. These vectors have been compared with other ice drift products of lower resolution, a sea ice model and data from drifting buoys in the north east Barents Sea. The SAR wide swath drift vectors agreed well with the buoy data on the one occasion a comparison was possible. They also proved to give more details and to be more exact close to land than lower resolution radar products. The validation of the model was useful, it was good in predicting the direction of the ice drift, however it was much too slow.

Following a ship drifting across the Arctic the manual ice drift vectors were used to study ice drift leading to deformation of the pack ice, so called differential ice drift. By colour coding drift vectors after length and plotting them on a SAR image, differential drift became apparent. It proved that the spatial resolution of the SAR images was enough to detect divergence and shear features only a few kilometres wide. Convergent motion could also be seen, but the subsequent ridging was difficult to spot due to the small size of ridges. The study also showed how quickly sea ice drift can change direction and speed, so to get a more complete picture of drift and deformation, SAR images should be acquired as often as possible.

During field work, measurements on sea ice were made, *i.e.* ice freeboard and thickness, snow thickness and density and ice density and salinity. These measurements showed that a method that is planned to be used from satellites to deduct the sea ice thickness was very sensitive to changes in snow depth and density. These are properties that can not be measured from satellites.

Contents

1

Introduction

This thesis is the final assignment of the MSc in Space Engineering program at Luleå University of Technology. The work was carried out at the Nansen Environmental and Remote Sensing Centre (NERSC) in Bergen Norway from August 2006 to May 2007. My supervisor at NERSC was research director Stein Sandven and my examinator in Luleå was Niklas Lehto.

Since the 1970's satellites have measured the global sea ice extent, and during this rather short measurement period the ice extent in the Arctic during summer has decreased dramatically. A decrease is something that all global climate models have predicted, but what have been seen is worse than all but the most pessimistic of the models [1]. This implies that our present understanding of sea ice is not good enough. A good sea ice model needs to accurately represent things like albedo, heat flux from both ocean and atmosphere and ice motion and deformation. For this many more observations are needed.

Unfortunately it is not that easy to extend the number of observations, the Arctic is far away and with a very inhospitable climate field observations are very expensive. In addition they only cover a small area over a short time period. To cover the entire Arctic, and to do it often, satellite measurements are needed. The polar night wintertime and the fact that the Arctic often is shrouded in clouds during summer, limits the usefulness of optical sensors. Longer wavelengths are needed, and when going to the microwave part of the spectrum, Synthetic Aperture Radar, or SAR, has a superior resolution to other instruments and is believed to provide better ice motion products than other sensors [2].

The objective of the thesis was to develop methods for monitoring sea ice using high resolution satellite SAR images from Envisat, to test the capability of the same images and to provide validation data for ice drift models. The chapters two and three of this report contains theory about both SAR and sea ice, to give a deeper understanding of the sensor that is used and the medium I look at. The chapters four and five contains the two data studies that I did, one of ice drift in the Barents sea and the other of ice deformation in the pack ice near a ship drifting across the Arctic. Finally I was privileged enough to be able to do field measurements on ice during a cruise with an Norwegian ice breaker around Svalbard in March 2007, chapter six is dedicated to this.

The different parts are not connected more than that they are on the same subject, but each part contributes with an understanding of the other parts, especially the fieldwork which gives an insight of what it really is that is studied on the satellite images.

2

Synthetic Aperture Radar

2.1 History

Satellite remote sensing has been around for almost 50 years. It is a part of everyday life by means of the weather satellites giving the basis of weather forecasts and it is important for studying all kinds of large-scale phenomenon in nature. Its ability to cover large areas continuously makes it an important tool for observing geophysical phenomena. The good temporal resolution near the poles makes satellites excellent tools for observing fast changing phenomenon like the variations and drift of sea ice. However, when it comes to observing the Arctic areas optical sensors are strongly limited by their inability to see through clouds and the fact that they are limited to daylight observation. By moving to the microwave area in the spectrum, these limitations can be overcome. The longer wavelength of microwaves penetrate clouds and microwave instruments are also not dependent on the sun as energy source for the radiation. Passive microwave sensors detect the black body radiation emitted from Earth, while active instruments send out their own electromagnetic waves.

Unfortunately it is not possible for a passive radiometer to achieve the fine resolution of the optical sensors, this is due to diffraction which is directly proportional to wavelength and inversely proportional to the aperture dimension. From a satellite with an optical system, resolution of a few tens of meters can be obtained with an aperture of some tens of centimetres. When wavelength increases the resolution get coarser unless the antenna aperture is increased with an equivalent amount. To get resolution of tens of meters with passive microwaves, the antenna aperture would need to be in the order of kilometres. This is of course not possible in a space borne radar, but in the 1950s Carl Wiley of the Goodyear Aircraft Corporation made the discovery behind Synthetic Aperture Radar (SAR) called Doppler beam-sharpening. He observed that the along track coordinate of an object can be acquired by analysing the Doppler shift of the reflected signal. This gave finer along track resolution than permitted by the width of the radar beam itself, which was the limit for side looking real aperture radars (SLAR) of that time.

In the following decades SAR was developed, mounted on air planes and eventually in year 1978 a SAR was launched into space on the satellite Seasat. It

was followed by a few other space shuttle based SARs in the 1980s. In the 1990s the number of satellite borne SARs increased significantly, with for example the Magellan SAR that mapped Venus. Today there are several active SARs circling the Earth, for example on NASA's Radarsat-1 and ESA's ASAR on board Envisat. They are important tools to, for example, observe phenomenon in the ocean, retrieve wind fields over open water and, as is done in this report, to study sea ice. In the near future both ESA and NASA are planning to launch new and more advanced SARs, to get continuous SAR-observations but also to get new products like for example high resolution altimeter data.

Most of the information in this chapter comes from the *Synthetic Aperture Radar Marine user's manual*, edited by Jackson and Apel [3]. For further reading on SAR it is recommended.

2.2 Principles of Radar and SAR

A radar is an active instrument which works by sending out pulses of microwave energy towards some scattering object and measuring the time it takes for the pulses to return. The number of pulses sent out per unit of time is called pulse repetition frequency, PRF. From the time it takes for a pulse to return from a scattering object, the range to the object can be determined. The spatial range resolution, dR, is determined by the pulse width τ according to the range relation

$$dR = \frac{c\tau}{2} \tag{2.1}$$

Where c is the speed of light. This means that even for a point scatterer the received signal will have an extension in time, τ the initial pulse length. To get a good range resolution (dR small) the pulse needs to be short. A very short pulse however means a system with large bandwidth as well as high amplitude, the latter since the detection possibilities of the pulse are determined by its energy. For a pulse short enough to give 10 m resolution the amplitude would have to be higher than a realistic antenna can handle. In order to avoid these problems chirped pulses can be used. A chirped pulse is a pulse where the frequency varies with time. In the case of radar application a linear variation is used, either increasing the frequency with time (up-chirp) or decreasing it (down-chirp). The chirped pulse is longer than a normal pulse, hence containing more energy at a lower amplitude. By keeping track of when a certain frequency is sent out and by frequency analyses find out when this frequency returns, the range of an object can be determined with a much higher accuracy.

In SAR and SLAR systems, the radar is mounted so that it is orthogonal to the trajectory of the satellite and side-looking, see Fig. 2.1. The range resolution of Eq. (2.1) can only be obtained when the target is orthogonal to the radar beam. In the case of side-looking radar there will be a projection factor in the resolution expression. This projection depends on the incidence angle θ_i of the radar beam, according to

$$dR = \frac{c\tau}{2\sin\theta_i}, \tag{2.2}$$

where i is a point on the ground between the near-range R_n and the far-range R_f. From Eq. (2.2) it is apparent that the range resolution at the near-range will be better than at the far-range.

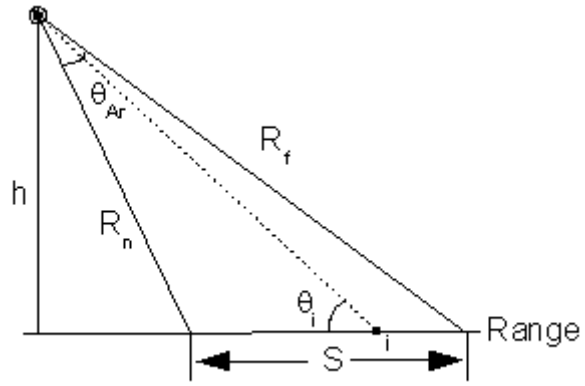

Figure 2.1: Range resolution for a side looking radar or SAR. The satellite is travelling out of the paper at the altitude h, with the radar is mounted so that is looks down to the left of the satellite with the beam angle θ_{Ar} and the swath S. The resolution at a point i between near-range R_n and far-range R_f depends on the angle θ_i.

The swath width, S in Fig. 2.1, is determined by the altitude of the satellite h and the angle θ_{Ar}. θ_{Ar} in turn is comes from the formula of the angle θ to the first minimum for diffraction through a circular opening of diameter D [4]

$$\theta_A = k\frac{\lambda}{D}. \tag{2.3}$$

The constant k is geometry dependant. A circular antenna would have $k = 1.22$ while other geometries will have other values.

The along track, or azimuth direction is acquired by the translation of the satellite. The radar sends out one pulse and from the return it forms a range strip. When the next pulse is sent out the satellite has moved, so a new range strip is acquired. Adding these range strips together builds up the azimuth dimension. In a SLAR the width of the strips, and thus the resolution, is determined by the diffraction formula in Eq. (2.3) multiplied with the altitude of the satellite. This gives coarse resolution for microwaves unless using an antenna which azimuth dimension is impractically large. Here SAR differs from other radars, and from where it get the name Synthetic aperture radar. It uses its forward motion to synthesise a much longer antenna and thus get an improved resolution.

In the book *Synthetic Aperture Radar - systems and signal processing* by Curlander and McDonough [5] a detailed description of how a SAR acquires its good azimuth resolution can be found. In simpler terms however, the motion of a SAR relative its target give rise to a Doppler shift of the return signal. This shift will be dependent on where in the azimuth direction the object is located. For an point object at slant range R and azimuth coordinate x, relative to the side-looking SAR (see Fig. 2.2) the Doppler shift relative to the transmitted frequency is

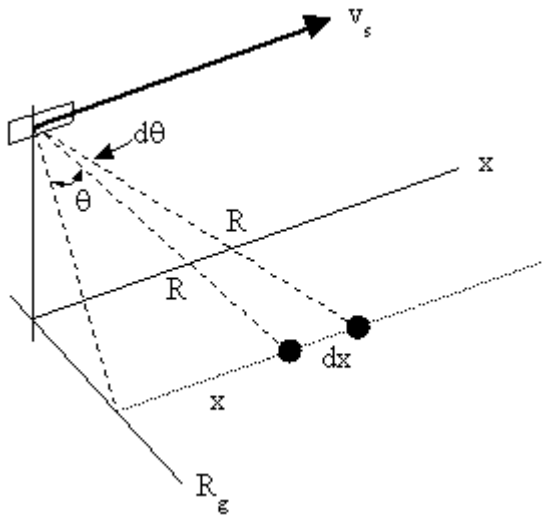

Figure 2.2: Azimuth resolution for a SAR. Two objects separated from each other with a ground distance, dx, at the same range, R, but with a difference in angle of $d\theta$ from the satellite will get a different value of the Doppler shift.

$$f_D = \frac{2v_s \sin(\theta)}{\lambda} \approx \frac{2v_s x}{\lambda R}, \tag{2.4}$$

where v_s is the velocity of the satellite relative to the target and θ is the angle off the broadside. This means that for two objects at the same range with a distance, dx, between them will have different Doppler shifts. Thus, even though the targets are at the same range and in the beam at the same time, they can be discriminated by analysing the Doppler frequency spectrum of the return signal. By combining the time delay of a pulse and the Doppler shift, a terrain point can be located in two dimensions. From Fig. 2.3 it can be seen that the range from a specific delay τ_0 and the Doppler shift f_{D0}, corresponds to, respectively, a specific circle and a hyperbola. These two graphs only intersect at four points in the plane of range R_g and along track distance x. By knowing which way the radar is looking the left-right ambiguity is resolved, while the point in front of the satellite and the point behind it will have different signs of the Doppler shift. The azimuth resolution dx is acquired by Doppler analysis of the radar returns, so it will be related to the resolution at which the Doppler frequency df_D is measured. From Eq. (2.4) the azimuth resolution is

$$dx = \left(\frac{\lambda R}{2v_s}\right) df_D. \tag{2.5}$$

The resolution in the frequency domain is the inverse of the time the signal can be analysed, that is the time it takes for the radar beam to pass over a target. This results in the following theoretical expression for azimuth resolution

$$dx = \left(\frac{\lambda R}{2v_s}\right)\left(\frac{L_a v_s}{R\lambda}\right) = \frac{L_a}{2}. \tag{2.6}$$

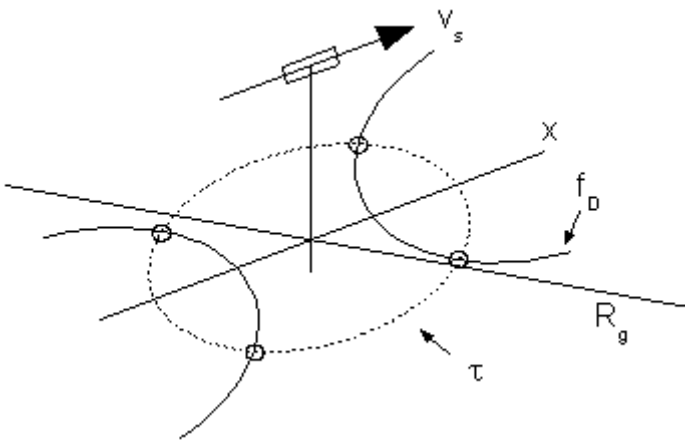

Figure 2.3: Iso-Doppler hyperbolas f_D, the iso-range circle τ and their intersection points. V_s is the satellite velocity and R_g the ground range.

Where L_a is the lenght of the antenna in the azimuth direction. This counter intuitive result, that a small antenna gives a better resolution than a large one, comes from Eq. (2.3) where it is stated that a small antenna gives a broad angle of the signal due to diffraction. A broad angle will in turn illuminate the object for a longer time. Typically a SAR sends out thousands of pulses that hits the object, each scattered signal from the object is recorded, with phase and amplitude, and in the process of creating an image all pulse responses from the object are summed up, giving a very strong gain and also good resolution. The longer time an object is illuminated by the radar the more pulses will hit and return from it, giving increased accuracy and hence better resolution. Needless to say, this synthesising is a computative very heavy process.

Although Eq. (2.6) implies that the azimuth resolution can be arbitrarily fine, independent of range, by just choosing a small antenna, there are of course limitations. Apart from the obvious limit that the size of the antenna determines how weak signals that can be detected, there are two conditions connected to how many pulses that are sent out per second, the pulse repetition frequency (PRF) which limits the resolution.

- In order to unambiguously sample the Doppler shift, the frequency bandwidth of the Doppler signal needs to be smaller than the PRF. This means that the radar must send out at least one pulse each time the satellite travels a distance equal to on half antenna length. Thus the lower limit of the PRF is given by
$$PRF > \frac{2v_s}{L_a}. \tag{2.7}$$

- To achieve unambiguity in the range direction only one pulse can be present in the target area at one time. Since the pulse gets wider from the scattering, the return from the near -range will come before the return from the far -range, the PRF must be low enough to avoid the end of one

pulse mixing with the beginning of the next. Hence the upper limit of the PRF must fulfil the condition

$$PRF < \frac{1}{2\tau + 2(R_f - R_n)/c}. \tag{2.8}$$

From Eq. (2.7) it can be seen that an increased resolution (smaller antenna in azimuth dimension) gives a higher minimum PRF, something which will eventually collide with the maximum PRF in Eq. (2.8) in the desire to get a wider swath.

2.2.1 SAR image characteristics

Geometric distortions

A SAR image can appear distorted compared to a photograph due to several of its characteristics. The resolution in range and azimuth for instance, is obviously dependent of different things, which means that a SAR sensor can have different resolutions in the two directions. Also, as can be seen in Fig. 2.1, the incidence angle varies over the swath. Since the range resolution is dependent on the incidence angle (Eq. (2.2)), the range resolution will be coarser further away from the nadir (right below) of the satellite. To get pixels of equal size a re-sampling of the image has to be done.

The location of an object in a SAR image depends on the range from the satellite to the object, called the slant range. The orthogonal distance from the nadir point of the satellite to an object is called ground range. If the satellite is flying over an area with mountains, the summit (B in Fig. 2.4) will be closer to the satellite in slant range than the bottom of the mountain (A). This means that they will, in the resulting image, be placed closer to the satellite then they are in reality b. This effect is called foreshortening. This can be clearly seen in SAR images where it looks like mountains are "leaning" away from the satellite.

In the slope from A to B many objects might be located at the same distance from the SAR in slant range. The result is that their backscattered signals will return to the antenna at the same time, giving a strong signal. If the slope is very steep, the response from B might even be return before A, so that b will end up left of a. This is called layover. More about geometric distortions can be found on the ESA Earthnet website [6].

Speckle and multilook processing

When imaging a region with SAR the size of a resolution cell will in most cases be large enough to contain multiple physical scatterers, each of size the order of the radar carrier wavelength (order of centimetres, but more about scattering further down). The transmitted radiation of a SAR is coherent, something that is necessary for the summations of the many thousands echoes each object gives rise to. Due to the coherent nature however, the multiple scatterers in one resolution cell give rise to constructive and destructive interference of returns, something that results in a grainy salt and pepper appearance to the image.

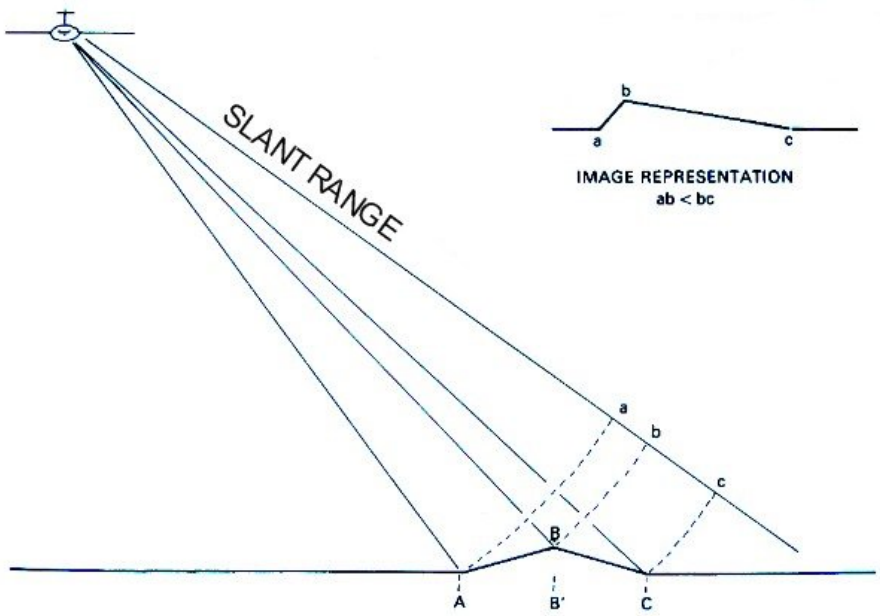

Figure 2.4: Distortion in SAR images. A mountain summit (B) is closer than its base (A) in slant range, this means that summit in the image (b) will be shifted towards the base in the image (a) and away from the far base of the mountain (c). This is called foreshortening. Figure from the Canada Centre for Remote Sensing [7].

This is called speckle and it is the same phenomenon as when pointing a laser at a white surface, darker and lighter spots are seen in the illuminated area

Since the speckle is produced by the scattering process it contains information of the scattering surface. However, the complexity of this scattering process makes it necessary to consider speckle as noise corrupting useful information [8]. One approach to reduce speckle is called multilook processing. As described on the ESA Earthnet website [6], when a SAR passes oven an area it collects many responses from every single object in the swath. It could use all of these responses to obtain the object's radar cross-section, this would give an resolution close to the theoretical value of Eq. (2.6). However, it would also produce quite a lot of speckle. In multilook processing, the data is processed in sections and then combined. For example, if 1000 samples are achieved per object, 250 of these can be used to determine an objects cross section. The next 250 samples can then be used for a second estimate and so on, ending up with four different estimates. By combining these four estimates, or looks, the speckle will be reduced. When an image has been processed as four-looks, the first quarter of the samples has been used to produce one image, the second quarter for a second image and so on. These four images has then been combined to produce the final result.

The multilook can be applied as any number of looks, the more looks the more is speckle reduced. This is due to the (apparent) random nature of speckle, one

pixel might be white in one look, but black in the next giving a grey pixel as result. Since less samples are used for each object however, the resolution will decrease with an increased number of looks, and other important information might be lost. There are constantly other methods being developed to reduce speckle while saving as much accurate information as possible [3].

2.2.2 Polarisation

Remote sensing radars are usually transmitting and receiving either vertically or horizontally polarised radiation. This means that the electric field of the wave is either in a vertical or horizontal (parallel to the ground) plane. The planes of polarisation is denoted H for horizontal and V for vertical. The polarisation modes for a radar image can thus be HH, for horizontal transmit and horizontal receive, VV for vertical transmit and vertical receive, HV for horizontal transmit and vertical receive and vice verse VH. When the polarisation of the received radiation is the same as for the transmitted, the image is said to be like- polarised. The opposite, when the received radiation has a different polarisation than the transmitted, is called cross-polarised image.

VH and HV modes will detect the radiation that has changed polarisation, something that typically happens in the case of multiple scattering due to surface roughness or multiple volume scattering. Cross-polarised images will be darker and show objects like forests (multiple volume scattering) and ice ridges (multiple surface scattering) more clearly than like-polarisation.

One difference between VV and HH polarisation can be exemplified with, *e.g.* a wheat field. If the wheat stalks are assumed to be short vertical dipoles, then the VV will interact strongly with them while the HH will pass unhindered and scatter from the ground. This is useful when studying the soil moisture. VV also gives a stronger signal from small ocean waves which can be used to extract wind speed. For the same reason HH is better to distinguish between water and sea ice, it gives a sharper contrast between what in a SAR image is dark sea and light ice. More details in polarisation is found in *Principles and Applications of Imaging Radar* by Deorowicz and Skorczynski [9].

2.3 Scattering

2.3.1 Penetration depth

The microwaves transmitted from a satellite borne SAR will propagate unchanged as long as they travel through a homogeneous medium. A change in electric properties, for instance when the wave enters a cloud, will refract the wave. The reason why microwaves, unlike optical light, can see through clouds is that the water droplets in the clouds are so small compared to the wavelength that the cloud will be a homogeneous medium for a radar wave, only refracting it slightly on entry and exit. For optical light however the cloud will consist of air mixed with water droplets with a size greater than the wavelength. Every boundary between different diffraction indexes which will give rise to refraction and reflection, ending up with the light being scattered in all directions.

When the microwaves reaches the ground they meet a boundary with different electrical properties than air. What happens to them depends on what material the ground consists of. The property that is the most important is the relative permittivity. It is a basic electrical property of all materials that affects the amount of an electromagnetic wave that is reflected, absorbed and dissipated. A material with high relative permittivity, *e.g.* sea water, will reflect most of an incoming radar wave at the surface so the penetration of microwaves into water is negligible. The distance an electromagnetic wave travels through a medium before its intensity is reduced by $1/e$ is referred to as the penetration depth, δ. This property is used to estimate where in a volume scattering may occur. Penetration depth is a function of radar frequency, incident angle and permittivity of the material, see SAR marine users manual chapter 2 for further reading [3].

A small penetration depth would mean that the incoming radiation is reflected at the surface, while an increased δ would give rise to scattering from inside the material.

2.3.2 Scattering mechanisms

Scattering of the radar waves from a SAR system is usually divided into two subtypes, depending on where the scattering takes place. The two types are surface scattering and volume scattering.

Surface scattering

When a microwave encounters a material with a low penetration depth, it will be scattered from the surface of it. Surface scattering is strongly dependent on the surface roughness and local slope and orientation of the surface. In fact, what is seen by a SAR in the case of surface scattering is surface roughness and not colours as in optical remote sensing.

The amount of surface roughness affects the distribution of the reflected energy, and thus the amount of radar backscatter. Whether a surface is considered to be rough or not when imaged by radar is a function of the radar wavelength λ, the incident angle of the radar beam θ_i and the average vertical displacement of the surface (rms height) δh. The criterion, developed by Lord Rayleight, where a surface is said to be rough if it meets the following condition

$$\delta h \cos\theta_i > \frac{\lambda}{8}. \tag{2.9}$$

In the case of Envisat ASAR with a wavelength of 5.7 cm and incident angle that varies between 15 and 45 degrees, a surface with rms-height of 1 cm and more would be considered rough.

For a smooth surface the scattering will be specular (like a mirror) and almost no radiation will return to the radar, while a very rough surface will scatter the radiation almost isotropically, see Fig. 2.5.

Bragg scattering is a very important case of surface scattering, it is the dominant scatter mechanism from the ocean for the incident angles between 15 and 70

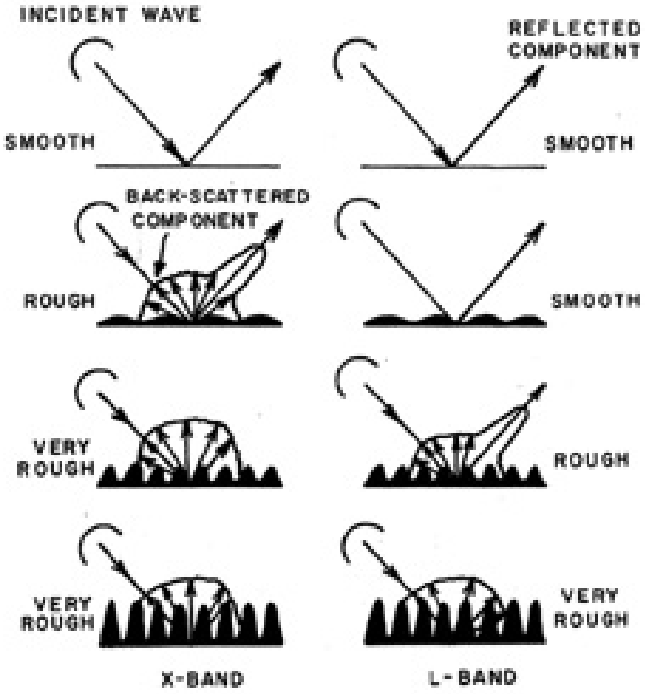

Figure 2.5: Scattering from smooth, rough and very rough surfaces. Whether a surface is rough is dependent of the wavelength which is scattering from it. X and L bands are short respectively long wavelength microwaves. Figure from SAR marine users manual [3].

degrees. When the wind waves increases to approximately the size of the radar wavelength, they become what is called Bragg waves. These will cause the scattered electromagnetic wavefronts to be in phase and add constructively, see Fig. 2.6, causing a strong return signal. The criterion for this to happen is

$$\lambda_S = n\frac{\lambda_r}{2\sin\theta_i}, \tag{2.10}$$

where n is an integer, λ_B is the wavelength of the Bragg waves, λ_r the wavelength of the radar and θ_i the incident angle. For Bragg waves all backscattered radiation will be in phase and thus interfere constructively, giving a strong backscatter signal. This is true for any n, but the dominant signal will be from $n = 1$.

Bragg waves are affected by larger waves, but also by phenomenons happening below the ocean surface, like internal waves, currents and ocean fronts. So even though microwaves only penetrates the upper few millimetres of the surface, these features can be detected in SAR images.

A vertical or close to vertical surface in an otherwise fairly flat area can give rise to *dihedral reflection*, see Fig. 2.7, giving a very strong return signal. This often occurs in urban areas, but also from ridges and ice bergs in sea ice. Here the orientation of the ice (ridges) plays a role. If the ridges are oriented orthogonally

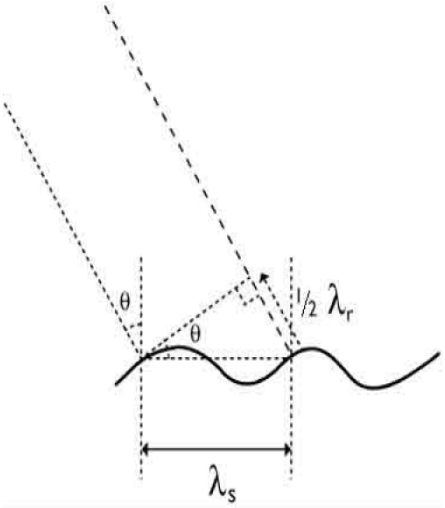

Figure 2.6: Bragg scattering. Two incoming rays are reflected off wave crests so that they returns in phase and thereby adds up constructively giving a strong return signal. θ is the incident angle, θ_S is the Bragg wave wavelength and θ_r is the radar wavelength. Figure from ESA Earthnet [6].

to the direction of propagation of the radar wave, a strong dihedral reflection is produced from the smooth ice into the ridge. If the ridge is oriented parallel to the view direction of the radar only the individual blocks within the ridge will give cause to dihedral returns, which results in a weaker ridge response.

Volume scattering

For materials with a high penetration depth, like fresh water ice, the micro waves will propagate into the material. If this material is inhomogeneous on the scale of microwave wavelength, *e.g.* ice containing air bubbles, the wave will be scattered from the dielectric discontinuities that the bubbles constitute. This is the same phenomenon as when optical light enters a cloud.

Assuming the scatterers inside the material are randomly distributed, the radiation from volume scattering will be in all directions and will thus give a strong backscatter compared to surface scattering.

2.3.3 Terrain reflectivity

Every material has an inherent reflectivity, an attribute just like colour or density. If a single point object, alone in its resolution cell, was observed several times from a specific incidence angle and with the same radar characteristics. it would get the same signature every time. In reality however objects are seldom point objects, therefore the inherent reflectivity is normalised per unit surface area, called intrinsic reflectivity, σ^0.

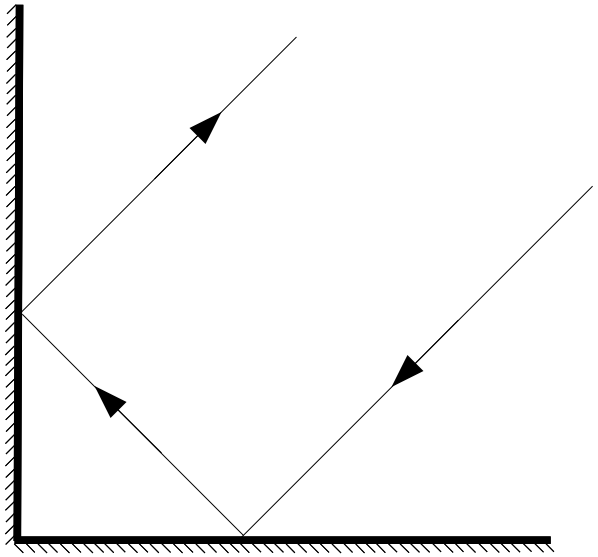

Figure 2.7: Dihedral reflection off a vertical wall.

To be able to get an estimate of the intrinsic reflectivity, the radar and processor has to be calibrated. The local incidence angle, that is the incidence angle relative to the local slope, also has to be known and corrected for at the scene location. If this is not known or if the system is not calibrated, a brightness estimate β^0 which is the mean power per pixel, is acquired. This brightness estimate is often corrected for slant incidence angle, or at least for the incidence angle in the middle of the image as is done by ESA. β^0 images is what is used for the data analysis in chapter three and four of this report. Further reading about terrain reflectivity can be found in the book *Principles and Applications of Imaging Radar* [9].

2.4 Envisat ASAR

All SAR-images used in part II and III comes from the ASAR (Advanced SAR) instrument on the satellite Envisat, launched in March 2002. It is a polar orbiting satellite dedicated to environmental studies to provide continuity of the observations started with the ERS satellites. Here follows a summary of different modes and products from ASAR, for further reading ESA Earthnet web pages [6] are recommended.

ASAR is a radar working in the C-band with a wavelength of 5.7 cm. It can collect data in pairs of the four polarimetric combinations. Its antenna is 10 x 1.3 m, consisting of many sub arrays each individually controlling the phase and amplitude of transmitted radiation. This makes it possible for the ASAR to operate in several different modes. These modes use two principal methods of measurements; it can operate as a stripmap SAR or as ScanSAR.

2.4.1 ASAR strip map modes

When operating as strip map radar the ASAR can image one of seven predetermined swaths, between approximately 56 km (for swath 1) and 100 km (for swath 7). This is done by changing the beam incidence angle and the elevation beam-width, also an appropriate value for the PRF is chosen. As a strip map SAR the ASAR can operate in two different modes, image mode and wave mode.

- Image mode: Image mode gives high resolution (30 m) images of any of the seven swaths in either HH or VV polarization. From this mode it is possible to get both multi-look images, good for deriving backscatter coefficients, and single look that is used for interferometric or wind/wave applications.
- Wave mode: The wave mode uses the same swaths and polarizations as the image mode, but it does not produce a continuous strip of data. Instead small areas, about 10 x 5 km, called imagettes are imaged at regular intervals of 100 km along track. These are processed to derive the spectra of the ocean backscatter and consequently the wavelength and direction of ocean waves.

2.4.2 ASAR ScanSAR modes

While operating as strip map SAR, the ASAR is limited to narrow swaths due to ambiguity reasons (Eq. (2.7) and (2.8)). This can be overcome by use of the ScanSAR principle. Unlike strip map mode, in ScanSAR the antenna is steered to scan so called sub-swaths long enough to get an image at desired resolution. Then it moves on to the next sub-swath. It continues in this way until the full wider swath is covered, then it returns to the first sub-swath and restarts the scanning cycle.

ASAR operates as ScanSAR in three modes, the wide swath (WS) mode, the global mode (GM) and alternating polarisation mode (APM).

- Wide swath mode: The WS mode uses five of the predefined swaths to get a total swath of 405 km with a resolution of 150 x 150 meters. It can be operated in either VV or HH polarization. Its wide coverage and medium resolution makes it very good for studying sea ice. Wide swath data is only collected when requested.
- Global mode: Like the WS mode, GM uses five of the predefined swaths with a total swath of 405 km. The produced images have a much lower resolution, about 1 km, with the same polarizations as for WS mode. The low resolution gives a much lower data rate, this means that global mode can be activated at all times and store the data locally until it can be sent down to a ground station. This is used whenever Envisat is flying over the poles to collect continuous ice images, unless any other product has been ordered.

- Alternating polarisation mode: Unlike the other ScanSAR modes, APM only scans between two different polarisations within one of the predefined swaths. This gives two images with a resolution of 30 metres over the same area in either HH/VV, HH/HV or VV/VH polarisation. This image pair can be combined in a similar way to spectroscopy in optical remote sensing.

2.4.3 Rolling archive

The ESA rolling archive consists of servers at the main ESA Envisat acquisition stations. This is where all systematic products (GM and wave mode) and also all, not just your own, ordered products are available for download. It contains products from about three hours after acquisition and stores them for 10 days. From here NERSC downloads all images in interesting areas to its own archive.

3

Sea ice

3.1 Background

Sea ice is one of the most varying geophysical features on Earth, it covers from 7 % of the Earths surface at minimum up to 13 % at maximum. However, due to the climate and remoteness of the polar oceans they are among the least understood regions of the planet, with very little acquired data.

Even though sea ice is thin, it only accounts for about 0.1 % of the Earth's permanent ice volume while it is about 70 % of its areal extent, it has a high impact on biological processes as well as for human activities in the polar regions. Sea ice strongly affects the local ocean-atmosphere processes, but it is also recognised as a key component of the global cryosphere and climate system.

There are major large scale differences between the two polar regions. The Arctic ocean is a deep basin centred on the North Pole and surrounded by land and narrow outlets into the Atlantic and the Pacific oceans. The ice in the Arctic can rotate in a big gyre for years before it leaves the basin through one of the straits. Thanks to this ice can survive for a long time, increasing its thickness and keeping parts of the Arctic ocean ice covered all year around. It also leads to a very compact ice cover with high internal stresses.

The southern ocean on the other hand, is a circumpolar ocean bounded in the south by the Antarctic continent. The atmosphere here is colder than in the Arctic, but the heat flux from the turbulent unprotected sea is much higher. This leads to an ice cover that is highly variable, wintertime it covers an area 50 % larger than the Antarctic continent while it almost disappears in summer. Since there is very little old ice, the thickness here is less than in the Arctic and the lack of restrictive land boundaries in the north gives an divergent motion of the ice cover. The result is significantly higher drift speeds than in the Arctic.

In many models sea ice is considered to be a smooth sheet of fresh water ice, but in fact sea ice differs a lot from that. It varies in thickness, it cracks open in leads or deforms in ridges. Not even a smooth area of sea ice is like the ice found on a lake. The salt in the ocean affects the freezing process, giving sea ice properties that differs much from those of fresh water ice. When studying sea ice it is therefore important to know about the material that is studied,

how it is formed and its properties but also its movement, distribution and transformation. More about the impact of sea ice can be found in the book *Polar remote sensing, vol.1 Atmosphere and ocean* by Lubin and Massom [10].

3.2 Ice physics

3.2.1 Growth of sea ice

Sea water freezing differs from the freezing of freshwater. The dissolved salt depresses the freezing temperature to about -1.8 °C (for a salinity of 33 ppt) [3]. The initial ice formation takes place at the surface, where the heat loss is greatest. Small platelets and needles, called frazil, begins to form. As these crystals grow numerous a soupy mixture of unconsolidated crystals and seawater is created, often referred to as grease ice (the light band in Fig. 3.1 a). With continued freezing under calm conditions the crystals begin to coalesce, freezing together to form a solid cover up to 10 cm thick. This thin hard ice cover is called nilas and is shown in Fig. 3.1 b). If wind and waves or waves are present, they will prevent nilas from forming, the grease ice will instead coalesce into small clumps that will later grow and harden into discs, see Fig. 3.1 c), named pancakes after their shape. By collisions with each other the pancakes grows bigger, up to 3 m in diameter. Between the pancakes slush is formed, either from frazil, snow or ablation from big floes. This slush will eventually consolidate and a solid ice cover is formed. As the ice grows thicker it is called first year ice (FYI), see Fig. 3.1 d). FYI can in the Arctic reach thicknesses up to 2.5 m [3].

Once the first ice cover has formed it will insulate the underlying ocean from the cold atmosphere, decreasing the rate of ice growth. Further ice growth must take place beneath this initial layer, something that most often occurs by sea water freezing directly to the bottom of the existing layer as the result of heat conduction upwards through the ice. This is known as congelation growth. The growth rate is in this case determined by the temperature gradient through the ice sheet and by the heat conductivity of the ice.

Crystal structure

Once the ice sheet forms and congelation growth starts, the crystals at the ice-water interface looses one degree of growth freedom. In order to grow without competing with other crystals they must grow perpendicular to the ice sheet, that is downwards. The result is a crystal structure consisting of vertically elongated columnar crystals aligned parallel to the direction of heat flow called columnar ice.

Ice that is not formed by congelation growth is called granular ice. In calm freezing conditions the layer of granular ice is very thin, but it can grow a lot thicker under other more turbulent conditions when big amounts of frazil ice is created. The frazil might form in depth in the water column, or be pressed under the surface in some way, and then freeze to the bottom of the ice sheet. Another mechanism that leads to granular ice is when a snow cover that has been saturated with water freezes and what is called snow ice is formed.

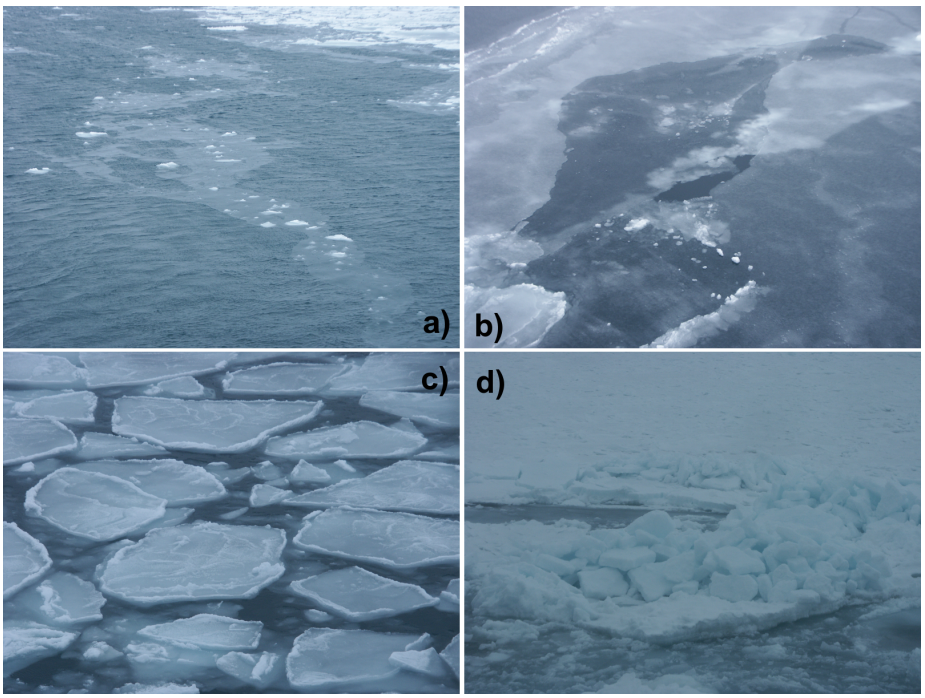

Figure 3.1: Different ice types. a) A band of grease ice, b) Rafted nilas, c) Pancake ice, d) First year ice with a ridge. Photos by the author.

Snow ice often has big grains and it contains plenty of air bubbles. Detailed information about ice growth and micro structure can be found in *Microwave Remote Sensing of Sea Ice* edited by F.D. Carsey [11].

3.2.2 Brine and air

The crystal structure in ice that freezes rapidly, as it does in the ocean, is too dense to accept salt ions. As a result of this, when sea water freezes, the salt is deposited and pure freshwater ice crystals are formed. The salt is dissolved in the water around the crystal, increasing its salinity and thus decreasing its freezing point. This high salinity water is called brine and is entrapped in all sea ice. For constant temperature the fresh water ice and the brine will always be in phase equilibrium, *i.e.* the local temperature in a brine pocket will always be that of the freezing temperature of the brine. If the temperature drops, some water in the brine freezes, more salt is deposited to the remaining brine depressing its freezing point. Thus a new equilibrium for the lower temperature is established. Since a temperature change always will lead to freezing or thawing in the ice it is, according to Notz [12], more correct to think of the ice as a two-phase two-component medium that does not have a fixed freezing point. This is also called a mushy layer.

In columnar ice the brine is entrapped as a part of the crystal substructure. Within each grain pure ice plates are separated by parallel layers of brine inclusions, that normally ranges from a few tenths of millimetres to about 1 mm

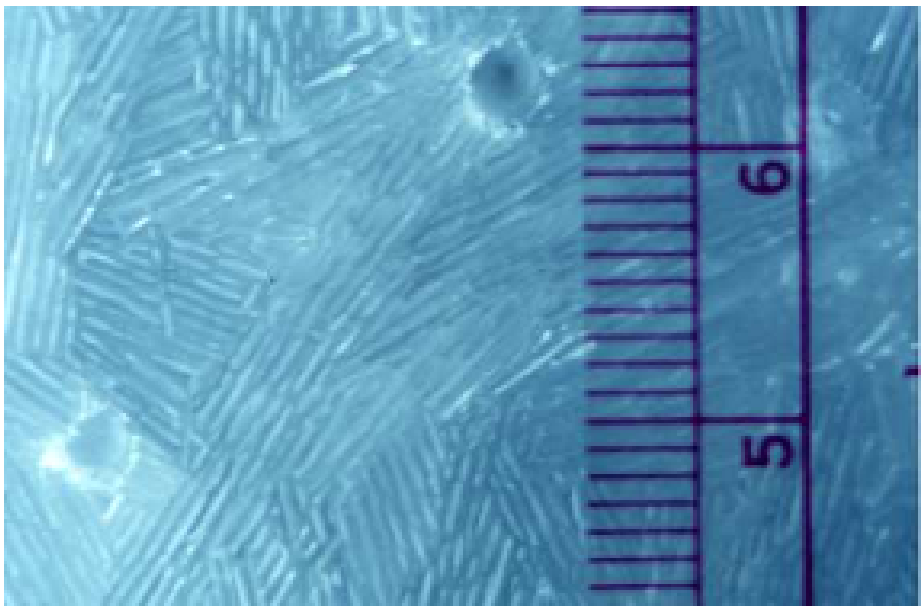

Figure 3.2: Cross section of ice grown in salt water in a laboratory experiment. The bright regions are solid ice while the dark areas are brine inclusions. Note how the bright ice plates have different orientation for the different ice crystals. Courtesy of John Wettlaufer, University of Yale [13].

wide, largely depending on growth rate. Each columnar ice crystal will thus contain several brine inclusions, see Fig. 3.2. In granular ice however, brine is not entrapped in a substructure as for columnar ice, but rather along the grain boundaries and at the intersection of grains.

The mixture of salt and air in the sea ice is very important to remote sensing, since the electromagnetic properties of the ice sheet, such as dielectric constant, reflectivity, volume and surface scattering, is heavily dependent on the distribution of brine and gas bubbles within the ice. This distribution is strongly affected by the temperature regime in the ice, both at the time of observation and at the time of formation of each layer in the ice sheet. The brine inclusion process is temperature dependent in that the plate spacing is almost solely determined by the growth rate. A faster freezing leads to narrower plate spacing which in turn entraps brine easier, resulting in higher salinity. Brine salinity of course also depends on the salinity of the water that freezes. Ultimately, the salinity of an ice sheet will be determined by the abundance of brine inclusions and the amount of solid salt and brine within these.

Since the most rapid freezing occurs at the top of the ice sheet, when there is less ice to insulate the ocean from the cold atmosphere, it is to be expected that the highest salinities are found there. This is generally true, however, a process called brine drainage starts as soon as the ice forms. Brine drainage is simply brine propagating from the top of the ice sheet further down and eventually leaving it. There are several mechanisms that has been said to explain this desalination, but according to Notz [12] the only mechanisms of any importance

are gravity drainage and flushing.

- Gravity drainage is the main mechanism for brine leaving the ice during winter. It is due to a temperature gradient in the ice where the surface of the ice is approximately at the same temperature as the atmosphere, whereas the bottom is at freezing temperature, about -1.8 °C. Since lower temperatures leads to a higher brine salinity, and thus higher density, this gradient leads to an unstable brine-density profile. The heavier brine in the top of the ice will act as a hydraulic pressure head and if the ice is permeable enough it will cause brine further down to leave the ice.
- Flushing is the most important process by which brine leaves the ice during summer. It is similar to gravity drainage, but instead of high density brine it is melt water lying on the ice surface that creates a pressure head driving the brine down through the ice. This process greatly decreases the salinity of the upper 50-100 cm of the ice sheet [11].

The result of brine drainage can be seen in Fig. 3.3. In October when new ice forms, the salinity is high with a C-shaped salinity profile that is typical for FY ice. With time, as the ice grows thicker, the salinity decreases through gravity drainage but the C-shaped profile is preserved. In June, when melting has started the salinity near the surface is drastically decreased by flushing. When the melt season has ended in August the desalinated layer has grown much deeper and the salinity further down is also decreased.

3.2.3 Multiyear ice

When spring melt sets in and the snow cover disappears, melt water covers large areas of the first year ice. Much of this water drains through the ice and the coverage decreases to about a third of the surface area. The greatly decreased surface albedo in these melt ponds increases the absorption of radiation and the ponds gradually grows deeper. On ice that survives the summer the melt pools eventually drains, leaving depressions that together with partly melted ridges gives the ice a hummocky appearance that is characteristic of multiyear ice (MYI). MYI is in other words first year ice that survives summer melt and starts on its second winter. For every freezing season MYI will get thicker until it reaches the thickness when, because of the insulating effect of the ice cover, winter growth is equal to summer melt. This is called the equilibrium thickness.

Both in the process of gravity drainage and flushing, brine channels are formed trough which the drainage takes place. These are vertical tubes up to tens of centimetres long and with a typical diameter of 0.4 cm [15]. As the brine flows downwards in the ice it will leave empty cavities behind and significantly increase the air content of the ice, especially after flushing. The drastic decrease of salinity trough flushing affects the upper 50 - 100 cm to down below 1 ppt from a normal value of FYI of about 8-9 ppt [11], see Fig. 3.3. This decrease of salinity which increases the penetration depth together with the increase of air bubbles, leads a change from surface scattering to volume scattering of microwaves, and thereby a pronounced increase in the SAR signature. The stronger backscatter from MYI makes it possible to distinguish between FYI and MYI in a radar image.

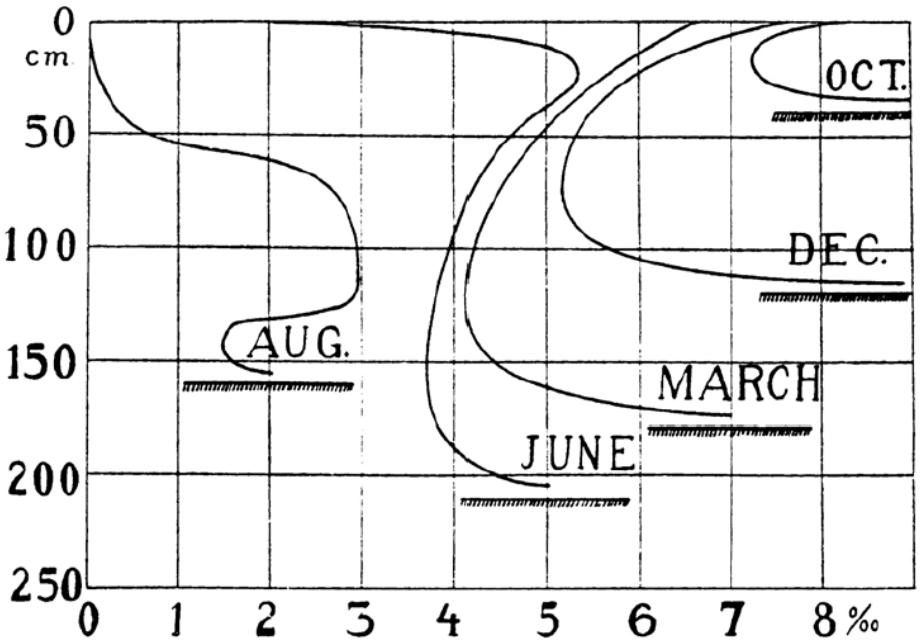

Figure 3.3: Salinity evolution of sea ice. From new high saline ice in October to ice that has survived summer melt and with the upper layer flushed free from brine. X-axis is salinity in ppt and Y-axis is depth under ice surface. Figure from *On the properties of sea ice* by Finn Malmgren [14]

3.2.4 Sea ice dynamics and motion

Until recently knowledge of sea ice motion has been based on drifting buoys deployed on ice floes, or ships freezing in and drifting with the ice. With instruments like space borne radars and IR sensors however, large scale ice motion products are now being produced on a daily basis.

Sea ice is almost constantly in motion, except in coastal regions where the ice is frozen to land (called land fast ice). Wind is the largest force that acts on an ice sheet, particularly responsible of ice motion on scales of days to weeks. The drag force depends on the surface properties of the ice, rough ice is more affected by wind than smooth ice, but the relationship between wind and ice drift is nonetheless so strong that the following general rule of thumb can be applied: Sea ice unaffected by *e.g.* land, drifts at approximately 2 percent of the wind speed and 20-40 degrees to the right (or left on the southern hemisphere) of the wind direction. This deviation in direction is due to the Coriolis effect that affects all large scale movement. Ocean currents also plays a role in sea ice motion, but with a smaller drag than from wind forcing it becomes an important factor on time scales in the order of months to years. On yet even longer time scales, sea surface tilt can affect ice motion. Sea surface tilt can be caused by things like tides, uneven heating and currents.

In compact ice, no ice floes can move without influencing the movement of other ice floes. This is called internal stress, it normally act as a resistance to motion caused by wind. Internal stresses are highly variable; ice is not very resistant to

tension forces so it is easily pulled apart forming fractures, but much stronger against compression so ice that is pushed against land by a strong wind might not move at all. It also depends on things like ice thickness, brine content of the ice, temperature and several other factors. Because internal stress varies so much it is difficult to make a good estimate of ice motion without it, but at the same time it is the most complex forces in an ice pack and it is the least understood.

It has always been known that sea ice moves on kilometre scales, but it was not until Fridtjof Nansen on board the ship Fram that it was confirmed that sea ice moves in large scale patterns too. In the Arctic there are two main large scale drift components (see Fig. 3.4), both wind driven. First the Beaufort gyre, a clockwise rotation around the north pole which results from an average high pressure system that creates the winds in the region. Second there is the Transpolar drift, where ice moves from the Siberian coast across the Arctic basin to the north coast of Greenland. Here most of the ice leaves into the North Atlantic through the Fram strait between Greenland and Svalbard.

Sea ice that forms or gets caught in the Beaufort Gyre might rotate around the Arctic for several years, giving it time to reach its equilibrium thickness. The circular motion in the gyre also leads to and increase of collisions between ice floes, resulting in a thicker and more deformed ice cover here than most areas in the Arctic. Sea ice in the Transpolar drift leaves the Arctic much quicker, usually in one or two years. Some of this ice is however pushed against the northern coast of Greenland and the Canadian archipelago, resulting in the thickest ice in the Arctic. For further reading on sea ice dynamics and much more, see the sea ice site of the American national snow and ice data center [16].

3.2.5 Deformation

There are several different causes of ice deformation. On the smaller scale, temperature changes in the ice makes it expand or contract with warming and cooling respectively, creating thermal cracks. These are normally in the order of tens of metres. In the marginal ice zone (MIZ), the transition zone between pack ice and open water, ocean waves are a major source of ice deformation. Short period waves are attenuated quickly by the ice, but long period waves can travel up to 500 km from open ocean and break the ice sheet [17].

Differential ice drift, when sea ice motion is not homogenous due to *e.g.* different wind forcing or internal stresses, is responsible for larger scale deformation. If this differential motion is convergent areas of rafting and ridging will be produced whereas if it is divergent leads will form. Differential motion can also cause shear zones which can include both areas ridging and lead opening.

Leads

A sea ice fracture is any break or rupture through ice resulting from a deformation process. Fractures range from small cracks on a few centimetres to formations several kilometres long and hundreds of metres wide. When a fracture is big enough to be navigated by surface vessels it is called a lead.

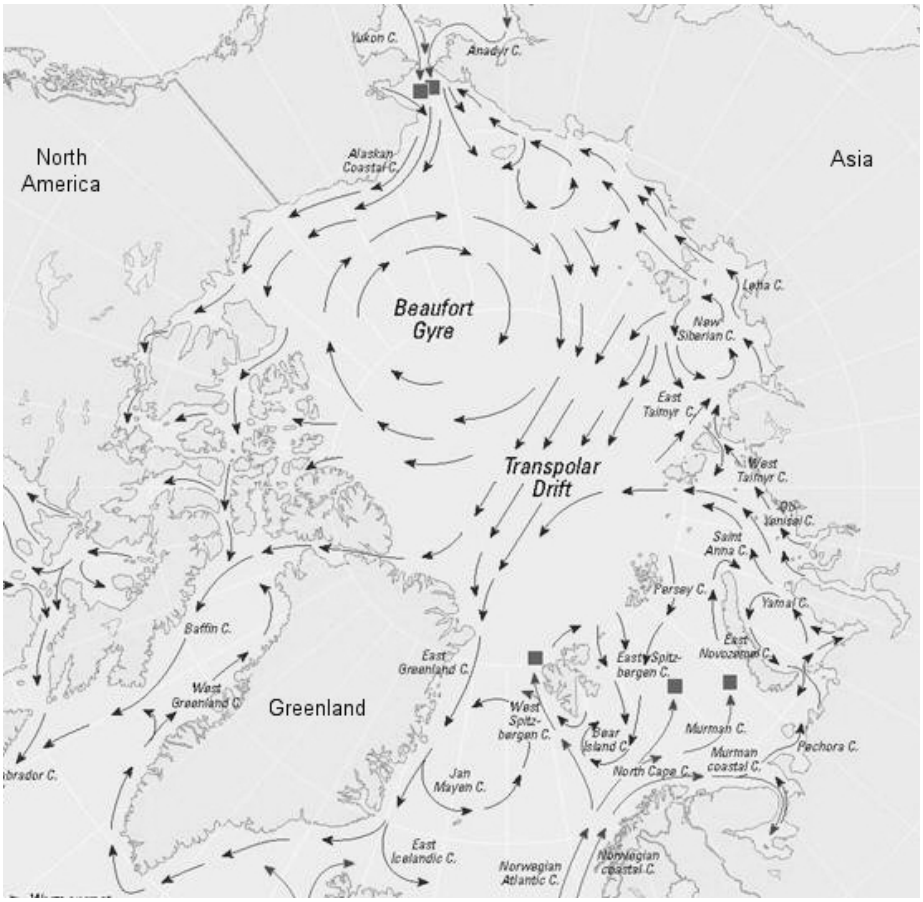

Figure 3.4: Large scale ice motion and ocean circulation in the Arctic. Image courtesy of Arctic Monitoring and Assessment Programme (AMAP), Figure 3.29, AMAP (1998).

Ridging and rafting

Ice deformation in a convergent ice field is called either rafting or ridging depending on the ice thickness. Thinner ice frequently breaks up by wind, waves or pressure from the thicker ice around it. Rafting is when a thin ice floe gets pressed up on another floe and thereby approximately doubling the thickness of the ice. Areas of rafting can extend for several kilometres with roughness up to a meter.

Thicker ice being compressed might break and form pressure ridges. Ridges constitutes of blocks that have been piled both above (Fig. 3.1 d)) and below surface and they can be up to 10 m high with keels deeper than 40 m. They are long and narrow, can extend up to several kilometres, although a few hundreds of meters are more common.

3.3 SAR signatures of sea ice

The properties of FYI, with a high dielectric constant and thereby a low penetration depth makes the surface properties of great importance for radar remote sensing. Surface properties depends on countless factors, but one important for the roughness are the conditions under which the ice was formed. Ice that has frozen under calm conditions will be very smooth and give an almost specular reflection with no return signal to the radar. If on the other hand the ice sheet forms in turbulent seas, the border between every consolidated pancake will be rough on scales equal to the radar wavelength, which results in a stronger backscatter. Other important things that affects the radar backscatter are snow cover and deformation features.

3.3.1 Snow cover and flushing

Dry snow is a mixture of air and pure ice, both with a low dielectric constant, so it is almost invisible to a radar. Indirectly however, the insulating effect of a snow cover increases the temperature at the ice surface which in turn increases the amount of brine in the upper part of the ice, decreasing the penetration depth. Wet snow is a different matter, already very small amounts of free water leads to a high dielectric loss which limits the penetration depth. As an effect of this a radar can no longer penetrate the snow and see the ice once summer melt sets in.

Snow can also affect the radar signature of sea ice in a more indirect manner. A thick snow cover can weigh down the ice so that it becomes flooded with sea water. The snow at the snow-ice interface will absorb the water, creating a rough and very saline layer which increases the scattering. When this snow-water mixture freezes an ice type called snow ice is created. Flooding of a multiyear floe will change the radar signature from volume scattering to surface scattering, making it look similar to a first year floe.

3.3.2 Ridging and leads

Rafting leads to an increased surface roughness which is seen as an increase in backscatter in the area while ridging is more prominent, standing out as long bright lines in a SAR image. How well a ridge appears depends on its orientation relative to the satellite. If the satellite flies along the ridge, a dihedral backscatter from smooth ice onto the ridge and then back to the satellite will take place, leading to a very strong signal. If the satellite flies across the ridge this dihedral backscatter will not occur. However as first year ridges are composed of angular ice blocks with the voids in between often filled with wind-compacted snow, the blocks can act as weaker dihedral reflectors.

Since fresh leads are just open water, they will look very different in a radar image depending on the wind conditions. In calm conditions when the surface is very smooth and acts like a mirror they will be very dark, but with just some wind, producing Bragg waves, they will be much brighter than the surrounding ice. However in winter time, a lead quickly freezes creating either nilas or pancake ice with their respective signature. On smooth thin ice in cold conditions,

frost flowers can form. These can be up to 6 cm high, being very rough on the radar wavelength scale, and can wick up brine from the ice they grow on. Once frost flowers become saline they produce a strong backscatter which makes the ice they grow on, often leads, look brighter than even MYI in an image. With time, the frost flowers breaks down by weather and wind and the backscatter is reduced to that of FYI. Refrozen leads are however weak spots in an ice cover, so any convergent ice drift normal to the lead will compress it and create a pressure ridge instead.

3.4 Impact of sea ice

3.4.1 Albedo

The albedo of sea ice is very high, often more than 0.85 with fresh snow, but it also varies a lot and can be less than 0.60 for melting ice or even less for bare ice [18]. During melt season it can vary even more, with melt ponds having an albedo of less than 0.20. This is a big problem when modelling the incoming solar flux, which is at its greatest when the albedo is the most unpredictable, so small errors in albedo have a big impact on the result.

Another important feature of sea ice albedo is its big difference from sea water albedo, which is about 0.07. This means that while sea ice reflects most incoming radiation, sea water absorbs almost all of it. In a scenario of a reduced ice cover due to increased temperatures in the Arctic, more radiation will be absorbed by the ocean, increasing its temperature and thereby reducing the ice cover even more. This is called the sea ice albedo-ocean feedback loop.

3.4.2 Ice thickness

Sea ice has a low thermal conductivity, even a thin layer of ice form an insulating barrier which greatly reduces the heat exchange between ocean and atmosphere, strongly affecting the Arctic climate. The effect sea ice has on the total heat budget of the polar regions depends very much on its thickness. The ice thickness is also the unknown parameter that is needed to calculate sea ice volume and thereby asses whether it is vanishing, and if so how fast it melts. This would give definite proof for a warming Arctic, and also valuable information to climate models.

Today thickness measurements are done by either using radar or laser altimeters and measuring the freeboard[1] of the ice and snow and from this calculating the ice thickness. A problem with this is that radar altimeters have a poor spatial resolution, and the only satellite borne laser altimeter, GLAS on board ICEsat is only operational a few months each year due to technical problems. The coming Cryosat II, which uses a SAR altimeter that will get good resolution altimetry data also in cloudy conditions, might be the solution of measuring ice thickness.

Another, simple way, is to classify the sea ice in terms of its age by looking at the brightness estimate, *i.e.* FYI is dark and MYI brighter due to the volume

[1] How much the ice surface is elevated above sea level

scattering [3]. This method is not at all as accurate as a direct measurement of thickness, but it has the ability to differ between softer thinner FY ice from thick and hard MY ice. This is important for sea-traffic operating in the Arctic, such as ice breakers and submarines.

3.4.3 Polynyas and deformation features

A polynya is any non-linear shaped persistent opening in ice [3]. Polynyas differ from leads in that they tend to recur and persist in the same locations over periods of weeks to months. They are lately classified after the location of formation as either coastal or open ocean polynyas. The coastal polynyas form where there are divergent ice motion conditions, typically down wind of stationary surfaces such as coasts, land fast ice or ice shelves. The ice that forms is these areas is blown away from the stationary surface and an area of open water is produced. Open ocean polynyas on the other hand results from upwelling of warm water that prevents ice from forming or melts existing ice [10]. The conditions in a polynya varies, containing everything from open water to pancake ice depending on weather and wind conditions.

The open water found in polynyas give rise to a strong heat loss from the ocean, so new ice forms rapidly. In the case of coastal polynyas where winds often being the cause of the open water, this new ice will be blown to one end of the polynya exposing the water to the cold again and more freezing takes place. This can lead to huge amounts of ice being formed in a polynya during its existence. Since ice formation leads to brine rejection, this type of polynyas produces large amounts of cold saline water that sinks to the bottom. The dense water will then start to flow downwards, providing a driving force for deep ocean currents, so this deep water formation is an important part in the global ocean current system, of which the Gulf Stream is a part. Polynyas are also very important for wild life, *e.g.* seals and polar bears. In the Arctic, the open water of polynyas inhabit plenty of life and are the equivalence to an oasis in the desert.

Leads, being much more abundant but smaller than polynyas, only covers a small areal fraction of the ice covered ocean. However they can dominate the regional ocean-atmosphere heat exchange in winter. Without an insulating ice cover there is a strong heat flux between the warm water and the cold air, warming the atmosphere and hence modifying mesoscale atmospheric motion. Once formed however, they quickly freeze forming thin ice that are weak links in the pack ice. Old leads are therefore the first to deform in a convergent ice field.

Ridges on the other hand covers a fairly large fraction of the ice cover for the reason that once they form they usually persists until they melt. The formation of ridges increases both ice thickness and strength, making it more resistant to melting. In other words an increased ridging leads to more MY ice. The fact that the thickest ice can be found north of Greenland, where it is piled up by the the Transpolar drift, and not north of Siberia where the lowest temperatures can be found, shows how important deformation is for the ice thickness distribution. Ridges also increase both the atmospheric and oceanic drag, something that influences the sensitivity of ice pack from both winds and ocean currents.

4

Sea ice drift analysis in the Barents Sea 2006

4.1 Background

The Barents sea, between Svalbard, Franz Josef Land and Novaya Zemlya, see map in Fig. 4.1 is a shelf sea with a high biological production thanks to the warm water masses coming from the Atlantic ocean. Except for the southern parts it is normally ice covered during winter, but in recent years a decrease of sea ice has been observed [19]. This decrease is of great interest for oil and gas companies, which in a future with less ice can exploit some of the large oil and natural gas findings in the area. For them sea ice drift in the area is of great interest and a good working model is very important. A model like this could be used to predict the drift of icebergs calving off the glaciers on Franz Josef land, and give early warning to manned platforms and sub sea structures.

For climate research, the straits between Svalbard - Franz Josef land and Franz Josef land - Novaya Zemlya gives the second largest contribution of ice transport out of the Arctic ocean, after the Fram strait. An accurate measure of this transport would give greater understanding of the heat balance in the Arctic basin, and thereby better climate models [10].

In early March 2006 three drifting buoys where deployed on ice floes in the area between Svalbard and Franz Josef land. The objective of this experiment was to measure the ice drift accurately using GPS positions, and to use these data for validation of ice drift derived from satellite data and ice drift simulations from models. On this background SAR data acquisition was intensified in the period March - April for estimation of ice drift from SAR data.

Figure 4.1: Map over the Barents Sea. The black polygon is the area where ice drift is studied.

The objective of the ice drift analysis is to

- Test the capability of high resolution ASAR wide swath images (WS) from Envisat to estimate sea ice drift
- Compare SAR WS ice drift with data for the three drifting buoys
- Compare SAR WS ice drift with Ifremer's[1] drift based on scatterometer and passive microwave data (Quikscat/SSMI)
- Perform the first tests of ice drift retrieval from ASAR global mode (GM) data and compare with WS data
- Validation of modelled ice drift from the TOPAZ forecasting system

The hypothesis is that SAR data can provide higher resolution ice drift fields than scatterometer or passive microwave instruments that is used by Ifremer to acquire ice drift, and also that SAR can provide data all year round. Another focus of the study is to compare the two ASAR modes, wide swath and global mode. Since the global mode data is continuously acquired from Envisat when no other products are ordered it provides a better temporal resolution, but the lower spatial resolution might reduce the quality of the retrieved ice drift.

TOPAZ is a data assimilation system for an ocean circulation and marine ecosystem model of the North Atlantic and the Nordic Seas with enhanced resolution in the European coastal zones. The assimilated data comes from satellite data available for real time operational use. It aims at providing real-time forecasts for both the physics and ecology of the North Atlantic ocean.

[1] French Research Institute for Exploitation of the Sea

Comparison of ice drift data with modelled ice drift from the TOPAZ system is important for validation of the forecasting capability of the sea ice model in TOPAZ. The ice drift modelling in TOPAZ is about to implement assimilating of drift data from Quikscat/SSMI, so a validation of this data is important to be able to appreciate the quality of the model [20].

4.2 Methods and results

The ice drift measurements was concentrated to the area shown in Fig. 4.1. containing the two big straits leading from the Arctic basin to Barents sea. A period of two months, March and April 2006, was studied.

Envisat ASAR global mode and wide swath images are continuously downloaded to a local archive on NERSC from ESA's rolling archive. From here wide swath images with coverage in the study area was chosen and ice drift calculated for three days intervals. Three days represent a sub-cycle of the Envisat orbit giving images over almost the same area. In addition to the wide swath images, ASAR global mode images were downloaded for the same dates when available.

Ice drift vectors were acquired manually by paring up two images covering the same area, the first called source image and the later target image, identifying structures and recording their position in both images. This was done using the program SARTool [21]. The error in recorded position is in the same size as the pixel size, that is 150 m for WS and about 1 km for GM.

In a few cases two scenes covering different areas of the NE Barents sea were available on the same day with only a few hours in between. The vectors from these two different image pairs are considered to be obtained at the same time. An overview of the image pairs used in the study, both for WS and GM mode images, and the number of acquired vectors for each image pair is presented in Table 4.1.

Ice drift data from Ifremer are based on scatterometer and passive microwave satellite data and are produced for the whole Arctic sea ice area and they come in a few different formats. In the study merged QuickScat/SSMI ice drift data was chosen, primarily because they come as three days drift, as was retrieved from the wide swath and global mode data, but also for the good amount of data in the relatively small area that was studied. These data were downloaded from the Ifremer website [22].

Ice buoy positions were provided by the Argos system, a satellite based location and data collection system operated by the French Space Agency, CLS. Argos receivers on board the American NOAA weather satellites provides positions of the Argos transmitters with an accuracy of 150 m [23]. Buoy data came in several positions each hour, but it was plotted as the drift over three days as in Fig. 4.3.

For visual comparison the WS vectors are plotted in the same map as the

1. Ifremer vectors, shown in Fig. 4.2.
2. Global mode and buoy vectors as in Fig. 4.3

Table 4.1: Dates with collected SAR data and ice-drift analysis.

3-day intervals	Wide swath		Global mode		Bouy data
	Time(GMT)	No of vectors	Time(GMT)	No of vectors	No of daily mean
2/3 - 5/3	16:24 - 16:30	21	08:08 - 08:14	4	
14/3 - 17/3	16:45 - 16:49	8	08:32 - 08:31	2	3
15/3 - 18/3	16:15 - 16:21	11	08:01 - 08:06	2	3
28/3 - 31/3	16:07 - 16:13	16			
29/3 - 1/4	15:36 - 15:41	9	07:14 - 07:19	10	
30/3 - 2/4	16:43 - 16:46	13			
31/3 - 3/4	16:13 - 16:18	17	07:59 - 08:05	10	
1/4 - 4/4	17:19 - 17:27	14	07:19 - 07:25	9	
10/4 - 13/4	17:39 - 17:42	2			
11/4 - 14/4	15:27 - 15:33	8	07:06 - 07:11	8	
12/4 - 15/4	16:36 - 16:42	11	09:54 - 10:00	1	
13/4 - 16/4	16:04 - 16:10	16	09:24 - 09:29	1	
14/4 - 17/4	15:33 - 15:38	9	07:11 - 07:26	5	
15/4 - 18/4	16:42 - 16:47	9			
16/4 - 19/4	16:10 - 16:16	11	07:56 - 07:54	5	
17/4 - 20/4	17:17 - 17:25	6	07:26 - 07:32	3	
25/4 - 28/4	16:27 - 16:33	8			
	Total:	189		60	6

The TOPAZ data was plotted in their own map due to the large amount of vectors it produces. It was compared with WS vectors plotted in another map with the same projection as in Fig. 4.4 and 4.5.

The general drift pattern during this period that could be identified was that during March the ice mainly drifted west or southwest through the strait between Franz Joseph land and Novaya Zemlya, while it in April shifted more to the west or northwest, with a few days drifting east out of the Barents sea. In the strait between Svalbard and Franz Joseph land the drift direction was more variable, but it was mostly southward during the measured periods in March and northward during April. The figures 4.2 - 4.5 are examples to highlight differences of the different methods, and are not representative for the drift pattern.

To get an overview of the quality of the different data sources, areas with uniform WS ice drift, that is WS vectors of the same size and direction, were picked out from each image pair. Within these areas, the average drift in kilometres and the direction in degrees clockwise from north was calculated for each data source. The results were plotted in two scatter plots, Fig. 4.6 for distance and Fig. 4.7 for direction. Due to the fact that the available satellite data covers different areas different days, the area of uniform ice drift varies between the different image pairs.

4.2.1 Discussion and conclusions

The amount of satellite WS images were, in spite of the increased acquisition, limited and the different image pairs covered several different areas. The WS-based ice drift vectors could therefore not be produced with regular spatial

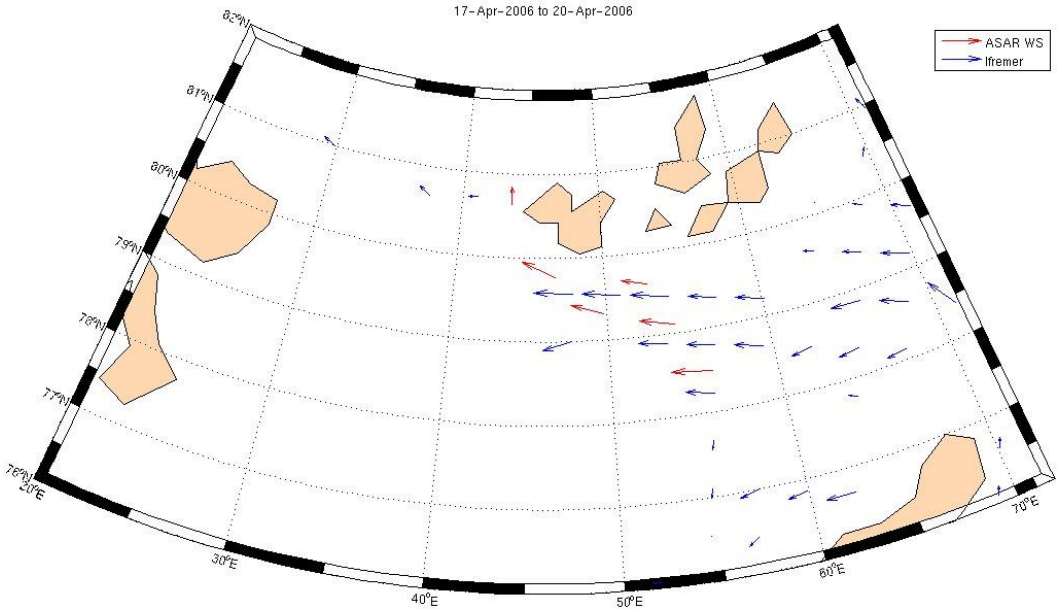

Figure 4.2: Ice drift from WS images and Ifremer scatterometer data between the 17th and 20th of April 2006.

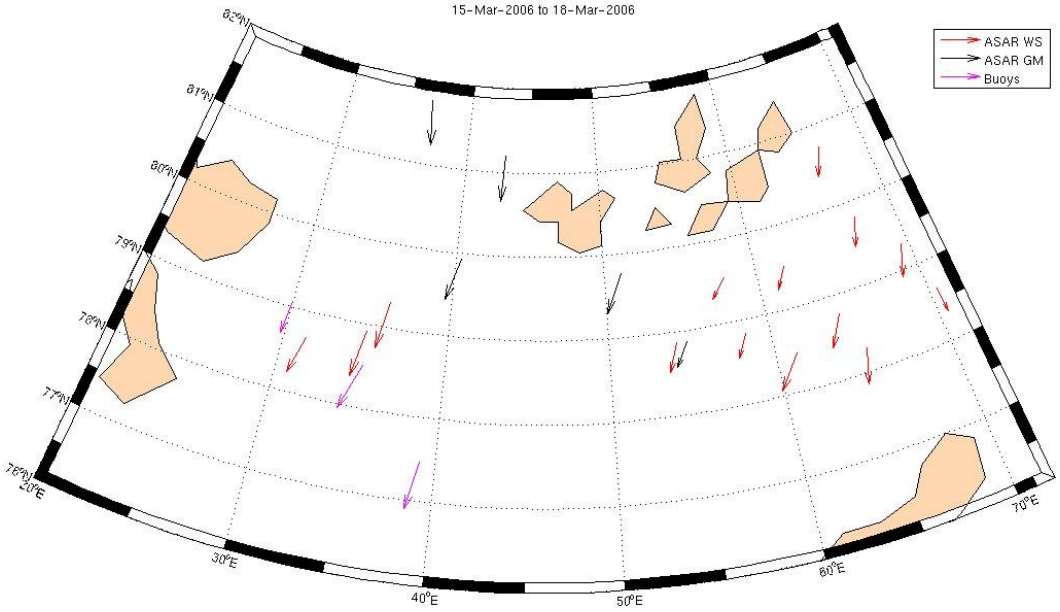

Figure 4.3: Ice drift from WS images, GM images and Argos buoys between the 15th and 18th of March 2006.

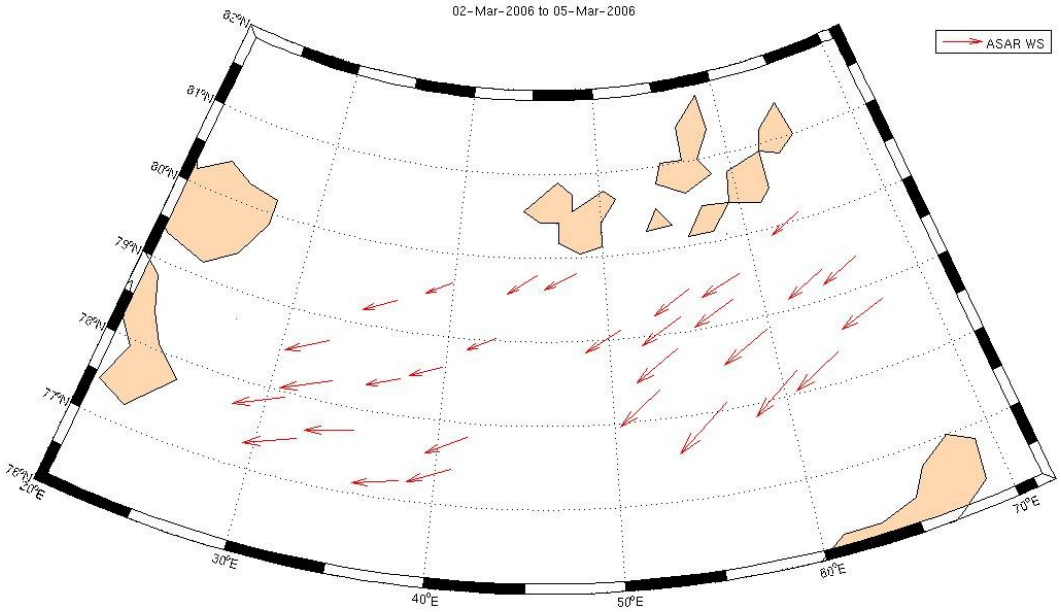

Figure 4.4: Ice drift from WS images between the 2nd and 5th of March 2006

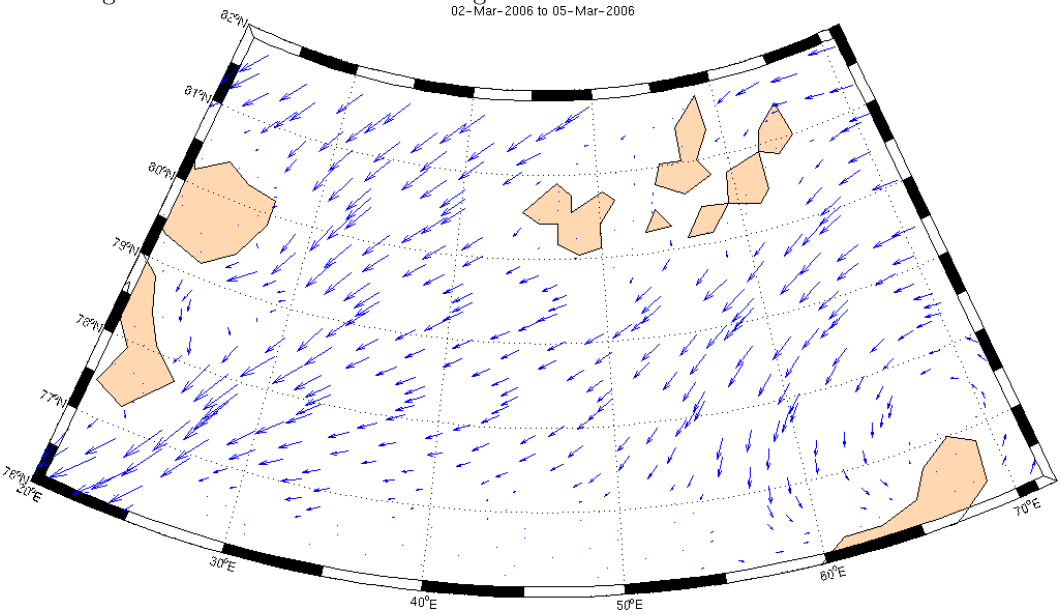

Figure 4.5: Ice drift from TOPAZ between the 2nd and 5th of March 2006

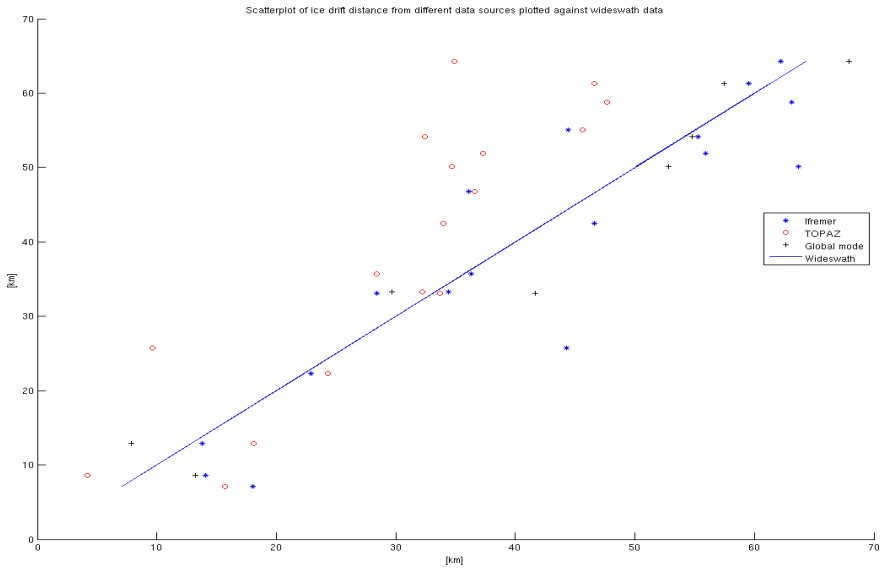

Figure 4.6: Comparison of drift distance between WS images on the y-axis and the other data sources on the x-axis. The closer to the line a marker is, the closer is the length of the vector of that data source to WS data. Vectors above the line are too slow, and vectors below it too fast.

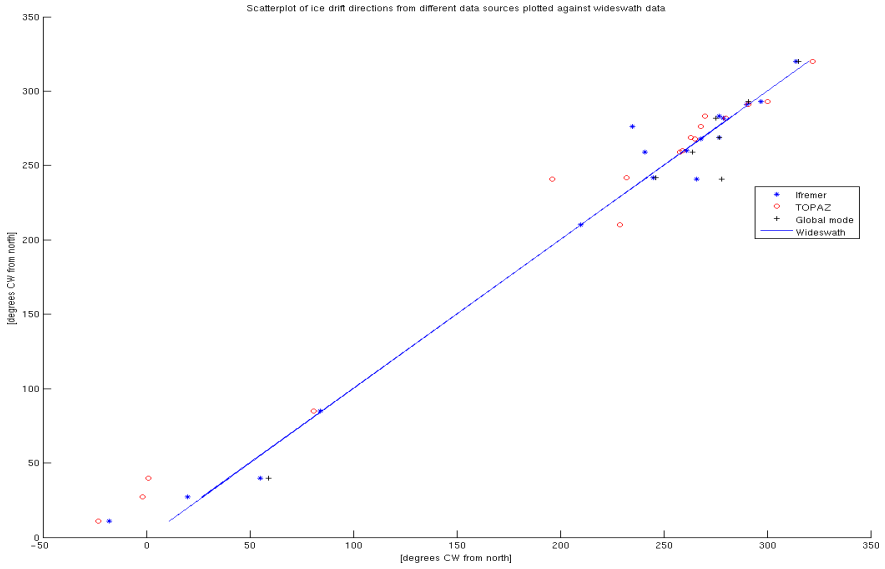

Figure 4.7: Comparison of drift direction between WS images on the y-axis and the other data sources on the x-axis. The closer to the line a marker is, the closer is the drift direction of that data source to WS data. Vectors above the line deviates to the left of WS vectors and vectors below the line to the left.

coverage in this region. The Ifremer products did also not provide full coverage of ice drift data, leaving many grid cells without data. Nevertheless, the satellite-based ice drift provided enough data to get an overall picture of the ice drift in the region, including the fluxes through the straits. The satellite data also provided a good data set for validation of the modelled ice drift from the TOPAZ forecasting system. Fig. 4.6 and 4.7 shows that the TOPAZ ice drift direction was quite good in the areas where comparison were made, but it underestimates the drift speed. Visual analysis of the vectors plotted in map projections confirms this for the entire area of study. The direction of the TOPAZ forecast is only obviously wrong in a few cases, while the drift speed is underestimated for the entire area for all time intervals.

The three buoys that were deployed drifted southwest reaching open water after a short time. Unfortunately the SAR images only covered the area where the buoys were during one period, 14:th - 18:th of March. This gave very little data for comparison, but as can be seen in Fig. 4.3 the SAR WS data shows good agreement with the buoy drift.

The Ifremer vectors shows good agreement with the SAR WS data, except for the region close to Franz Joseph land where the ice drift sometimes had a NW direction that Ifremer data did not always catch, see example in Fig. 4.2. This could be because of the coarser resolution satellite data that Ifremer is based on. Near coast lines, ice deformation rate is higher than in open ocean, so larger features that can be resolved by a scatterometer are broken down rapidly and therefore less common. Earlier studies have shown that the Ifremer ice drift was less accurate compared to SAR derived ice drift in other areas of high deformation, such as the Fram strait [2]. In the marginal ice zone, neither Ifremer nor SAR ice drift products provided any vectors. The reason for this is that on satellite images visible features in the ice are destroyed by the movements of the ocean so that a feature found in one image can not be identified in another image a few days later.

In the comparison between ASAR wide swath and global mode data, the wide swath proved to be significantly better, with more vectors for each image pair and with the vectors being more accurate. In the 12 cases where the two data sets were compared, WS provided 141 drift vectors while GM only provided 60. Under some conditions, when the texture of the ice was fine, the global mode images could not be used to provide manual drift vectors at all. This result is not surprising since the higher resolution of WS images resolves more details of the ice cover, such as leads and floes, that are needed to retrieve ice drift manually. In this study, SAR acquisition in the area was intensified, so the access to WS data was not a problem. However, in other cases it might be impossible to get the amount of WS data that is wished for, and in these cases global mode data can provide accurate ice drift. As can be seen in Fig. 4.6 and 4.7 both distance and direction are close to that of the WS data. The density of drift vectors from GM images will however be lower, and it could be difficult to detect smaller scale movement.

The first study of ice drift with SAR data in the northeastern Barents Sea showed good agreement with other ice drift data provided from scatterometer and passive microwave data as well as with buoy drift data. Satellite data can provide a reasonably good picture of the ice drift over large areas, in contrast

to drifting buoys which can only provide data in a few locations depending on how many buoys that are in operation. Buoy data however, provide continuous and very accurate measurements of the ice drift.

4.2.2 Future work

This study has used three day interval for the ice drift, but it is necessary to compare with daily averaged ice drift because ice motion can change rapidly because of changing winds. The manual analysis done in this study is an accurate method of acquiring ice drift vectors, however it is very slow and repetitive. An automatic analysis, done by letting a computer correlating two images, would give continuous and accurate measurements on a daily basis.

Data on sea ice drift will be an important component of the validation of models that are run at NERSC, *e.g* an iceberg drift model. Icebergs are difficult to detect by remote sensing, so drift can currently only be obtained by deploying Argos/GPS drifters on selected icebergs. However, the iceberg drift is a function of the sea ice properties such as concentration, thickness and speed. The goal for this model is therefore to come up with a monitoring and forecasting system for sea ice and icebergs, using numerical models in combination with satellite data and drifting buoys.

The data set in this report is the first validation of the ice drift model in TOPAZ. To be able to find out why the model underestimates the drift speed and whether this underestimation is season dependent or a general bias, more data is needed over the entire year, preferably acquired by an automatic computer analysis.

5

Differential ice drift around Tara

5.1 Background

Tara is a sailboat constructed to be able to be frozen into the ice. As a part of the EU project DAMOCLES [24] it was anchored in the Arctic pack ice in the Laptev sea north of Siberia in September 2006. The plan was that Tara would follow in the footsteps of Fridtjov Nansen and his ship Fram and drift with the Transpolar drift until it exists the pack ice north of Svalbard. The expected time for this journey is about two years. The main objective of Tara-Damocles is to increase the understanding of global warming in the Arctic concerning sea ice cover, atmospheric key processes and ocean circulation, all in order to improve present simulations of a changing climate.

At the Nansen centre ASAR WS images of the area around Tara were ordered weekly with the objective to study ice drift and differential ice drift on small scales and also to test the capability of SAR WS images to do this. Linear deformation features like ridges and leads play an important role in the dynamics and thermodynamics of sea ice, so to make an accurate ice dynamics model for climate studies the appropriate proportions of these processes must be known. Work on a large scale has been done by Kwok [25] where he looked at the entire Arctic, but not on smaller scales.

From the middle of April SAR WS images became available daily, so a study how daily drift compares to weekly drift was also made.

5.2 Methods and results

This study is divided in two parts, one where differential ice drift around Tara is studied and one where daily ice drift is compared to drift over a longer period. The daily drift is also compared with wind data.

5.2.1 Sea ice deformation

In the period 1st of October to the 31st of March a total of 27 scenes containing Tara were obtained. Of these, 24 had a resolution and image quality good enough to be used for high resolution ice drift. These are listed in Table 5.1.

Table 5.1: ASAR scenes containing Tara.

Date	Start time	Date	Start time
01 Oct.	09:49	21 Dec.	10:44
03 Oct.	10:26	24 Dec.	10:49
06 Oct.	10:32	15 Jan.	09:18
09 Oct.	10:37	22 Jan.	08:58
12 Oct.	10:43	29 Jan.	08:38
07 Nov.	10:26	20 Feb.	05:27
10 Nov.	10:32	27 Feb.	05:07
23 Nov.	10:24	07 Mar.	05:56
26 Nov.	10:29	17 Mar.	07:21
08 Dec.	10:52	24 Mar.	07:01
11 Dec.	10:58	31 Mar.	06:51
18 Dec.	10:38		

In an area about 150 x 150 km centred around Tara ice drifts vectors were acquired with the same method as in chapter 4. The goal was to get an even coverage of the area and to have as many vectors as possible, which is most cases meant between 10 and 30 vectors for each image pair.

In the beginning of the period, until the 26th of November, large differences in drift length and direction could be found, with a maximum difference of 7 km between slowest and fastest vector in the drift between the first and third of October (Fig. 5.1). In this period the drift was divergent in some areas due to differential direction but convergent in others due to differential speed.

To detect any differential ice drift the ice drift vectors were plotted with an $'o'$ at the start point and a colour code corresponding to its length, see Fig. 5.1, 5.3, and 5.4. This way both different directions and drift speeds can easily be seen. These vectors were plotted on the target image, so that any deformation of ice that had taken place during the interval between the images could be seen. In the same images, the start $'o'$ and end $'x'$ position of Tara and also its daily drift during the interval between the scenes were plotted, to get an idea of the real ice motion between the two images. Tara position data comes from Leif Toudal at the Technical University of Denmark.

From the 26th of November and forward the ice drift was fairly uniform until mid March, with the exception of two periods, 24th of December to 15th of January and 22nd to 29th of January. Between the 17th and 24th of March the ice pack changed direction abruptly several times as can be seen on the Tara trajectory in Fig. 5.3. The resulting ice drift is small, only 2-4 km but in three different directions with a resulting shear and divergence zone going through the entire image from north east to south west. This was in fact a part of a big shear zone more than 500km long varying between 5 and 15 km wide stretching from SW to NE. In Fig. 5.3 the main shear branches and a smaller part (both

marked with yellow) travels more to the south. This smaller branch is less than 3 km wide. In the following period, 24th to 31th of March, the lead closes. This can be seen in Fig. 5.4 where drift vectors on the right side of the image are longer than on the left giving a convergent motion.

A total of 22 scenes with ice drift were obtained, of which 10 scenes, presented in Table 5.2.1, showed significant differential ice drift. Four of these were due to a shear motion, of which one also containing a divergent area. Of the remaining scenes two were convergent, one divergent and one containing both convergence and divergence. In the two periods 9th - 12th of October and 12th Oct - 7th Nov differential ice drift was found, with the fastest ice moving more than a kilometre per day faster than the slowest ice, but no deformation zone could be identified. On the image of the 7th of November plenty of white lines can be found (see Fig. 5.2), implying that the differential ice drift has led to ridging.

The reason for the differential drift was either differential direction, when not all the ice was drifting the same way, or differential speed, when one area drifted faster than another. The width of the deformation zones varied between 3 and 20 km with a shear zone far into the pack ice being the narrowest and a divergence zone close to the ice edge the widest.

Table 5.2: Periods with differential ice drift. Width is the with of the deformed zone and the last column is the cause of the differential drift.

Date	Type	Width	Differential
1-3 Oct 2006	Divergence	20 km	Direction
	Convergence		Speed
3-6 Oct 2006	Convergence		Speed
9-12 Oct 2006	?		Speed
12 Oct - 7 Nov 2006	?		Speed
10-23 Nov 2006	Shear	15km	Direction
23-26 Nov 2006	Shear	15km	Speed and direction.
24 Dec 06 - 15 Jan 07	Shear	10km	Speed
22-29 Jan 2007	Divergence	10km	Speed
17-24 Mar 2007	Shear	3 km	Direction
	Divergence	5-10 km	Direction
24-31 Mar 2007	Convergence		Speed

5.2.2 High temporal resolution drift

In the end of April, when Tara had drifted too far north for the ASAR on Envisat, NERSC received SAR images of an area in the Laptev sea south of Tara. In the time period 17th to 30th of April there were daily coverage, sometimes several images per day, with the exception of the 22nd when no images were acquired. This opportunity was used to study ice drift over short time scales and to compare ice drift with wind speed and direction.

Thirteen images were picked out, one for each day except the 22nd, and all acquired between 7 am and 10 am. Ice drift vectors were acquired manually in the same way as before, but now seven distinct features were followed through the period. Two of the features could not be identified in all images, so on those

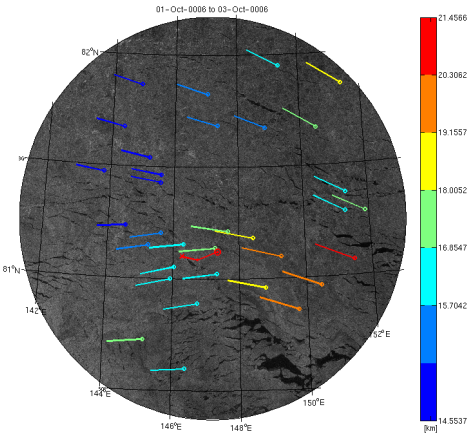

Figure 5.1: Differential ice drift, 1st to 3rd of October 2006. The area is close to the ice edge and leads, the dark lines in the image, are abundant. Large differences in vector length are present.

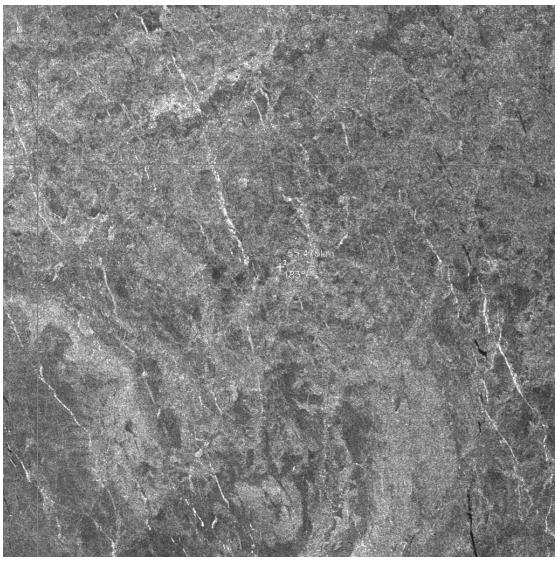

Figure 5.2: SAR image over Tara the 7:th of November 2006. The white lines going from top to bottom of the image are possible ridges. Tara is positioned in the centre. Image is 150x150 km.

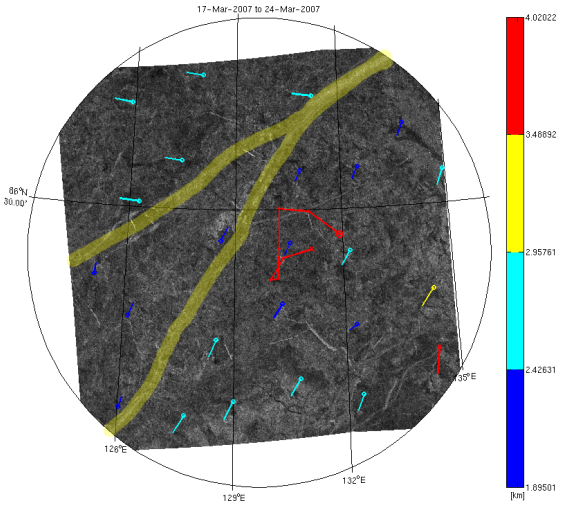

Figure 5.3: Differential ice drift, 17th to 24th of March 2007. Yellow lines marks areas of deformation, the upper line is a lead opened by divergent motion and the lower line is a shear zone.

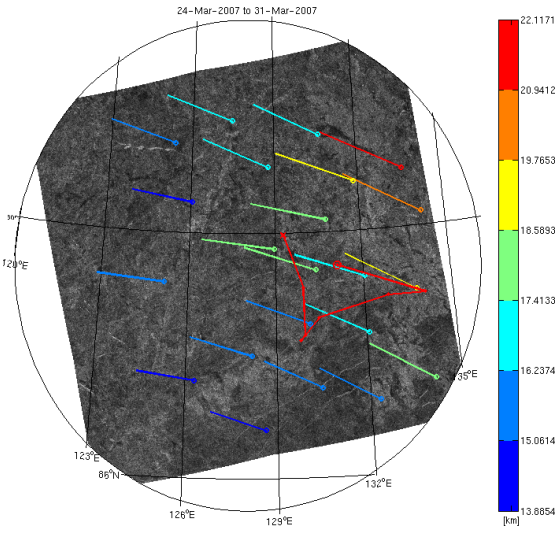

Figure 5.4: Differential ice drift, 24th to 31th of March 2007. Convergent motion where the lead from the 17th to 24th of March is closed.

days a nearby feature was used instead. In Fig. 5.5 the ice drift for these seven features are plotted, with small blue arrows for the drift from day to day. The resulting drift from the 17th to the 30th of April is plotted with thick arrows.

The first day the ice drifted towards NNE to turn towards N and NW the following two days. From the 20th to the 23rd the drift turned to SW to later go back to N. From the 24th and forth the drift changed slowly towards east.

For the same area, daily wind data was obtained from NCEP [26] at 23 points along latitude 84.75N and 23 points along 86.65N. NCEP data is assimilated, a melding between model and observational data, and is provided by the *NOAA/OAR/ESRL PSD*, from their Web site at `http://www.cdc.noaa.gov/`.

The average of the 64 data points were calculated for each day in u (eastward) and v (northward) wind components and the same was done for the seven ice drift data points. From these u and v components the magnitude and direction of wind and ice drift was calculated and plotted together in Fig. 5.6.

It is a strong correlation between wind direction and the direction of the ice drift. With the exception of the 19th and 20th of April the ice is drifting with an angle to the right of the wind, as should be expected on the northern hemisphere due to the Coriolis effect. From the 24th when the wind was not changing very quickly the drift was offset between 12 and 19 degrees to the right of the wind direction. The magnitude of the ice drift follows the wind fairly good except between the 18th and 19th. The correlation between wind strength and ice drift magnitude is however not as strong as the direction.

5.3 Discussion and conclusions

Tara is drifting much faster than its predecessor Fram, so fast in fact that it will leave the ice as much as 6 months earlier than expected. Why is not clear, no articles has yet been published, but it could have to do with the fact that the sea ice extent in June 2007 was the lowest since measurements started [18]. This could possibly give less internal stress and more mobility to the ice cover.

In this study the higher amount of differential ice drift is in the beginning of the period. This is likely because Tara was close to the ice edge but as it got further into the pack ice the increased internal stresses made ice motion more homogenous. The size of deformation zones has also decreased with an increased distance to open water.

From the studies of short timescale drift and from the trajectories of Tara, especially in Fig. 5.3, where a small resulting ice motion is present but with a significant motion of Tara, it is obvious that ice drift changes rapidly. To acquire ice drift from images with a week in between will give the total ice drift over this time period, but it says nothing about what happens in between. The figure 5.6 implies that the ice drift is strongly dependent of the wind.

The detected deformation is mainly shear or divergent motion. The width of the deformed areas is similar both for shear and divergence, but the shear zones were much longer. It is not always obvious what type of motion that causes the deformation, *e.g.* the divergence in Fig. 5.3 is a part of a large shear motion which in the small area of the study looks like divergence. Convergence was

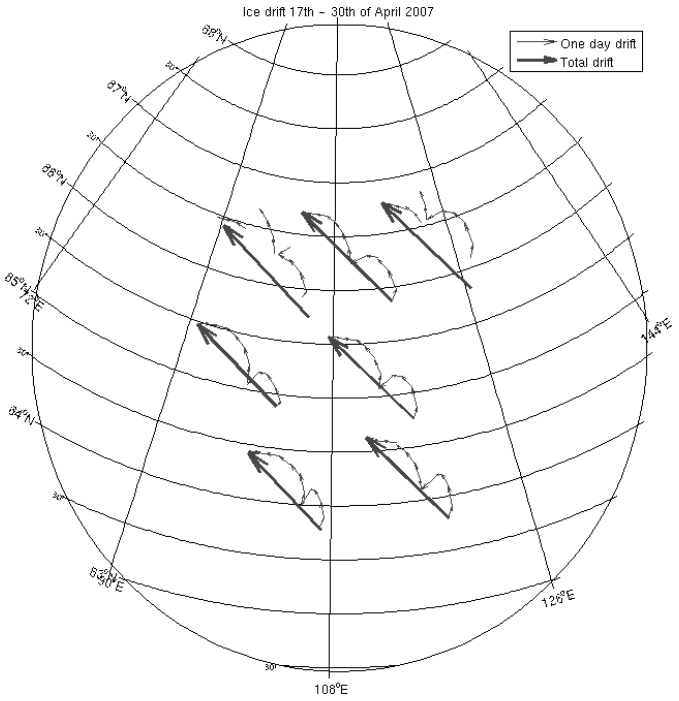

Figure 5.5: Ice drift 17th to 30th of April 2007. Small arrows shows daily drift and the thick arrows the total ice drift of the period.

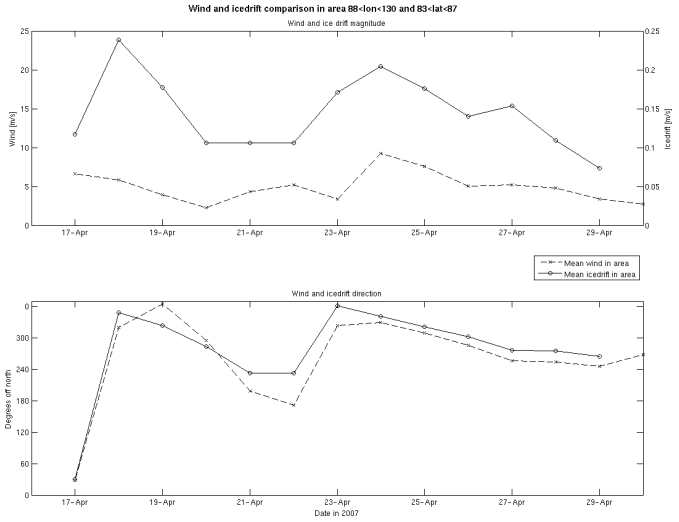

Figure 5.6: Ice drift magnitude and direction plotted together with NCEP wind magnitude and direction. Please note that the magnitude scale is different for wind and ice drift.

difficult to detect, in a few cases (*e.g.* Fig. 5.1) the plotted ice drift implied convergence, but no features of the ice verified this. The reason is probably that for a ridge to be clearly seen with the used resolution it needs to be oriented so that it gives dihedral backscatter, or it will just give a slightly increased signal. In the image from the 7th of November (see Fig. 5.2) several white lines that could be ridges were visible. Due to the possible ridging which changed the texture of the ice, it was hard to recognise any features from the image taken a week before, so no drift data could be acquired in the relevant area to confirm convergent motion.

In this study no old shear zones sheared again, but divergent features like leads tended to close by convergent motion not long after they were formed. In fact, the cases where a lead that was opened by divergent ice drift during one image pair, and then closed in the next pair, were the only cases of convergent drift that lead to visible change of the ice texture. An example of this is the figures 5.3 and 5.4, where the lead in the first figure is closed in the latter. By summing the vector length in the two images, on the left and right side separately, it seems like the total ice drift from the 17th to the 31st of March is almost uniform or even slightly convergent. All this indicates that the opening of leads is a fast changing phenomenon that can be missed completely when having too long time between observations.

The spatial resolution of SAR images is high enough to detect at least divergent and shear motion of the ice, but with the quite low temporal resolution that was used near Tara, things like lead openings and closings might be missed completely. A high temporal resolution is no problem to get on latitudes as high as where this study was made, however it means many expensive satellite images need to be bought, something that few can afford. Another problem for finding deformation with this method of looking at ice drift vectors, is that it is easiest to get vectors in ice that preserves its features between the images. This is not the case when ice deforms, so a bias towards undeformed ice is easily introduced.

6

Ice measurements on the K/V Svalbard cruise in March 2007

6.1 Background

From the 19th to the 31st of March 2007 the Norwegian ice breaker KV Svalbard went on a cruise around Svalbard, from Longyearbyen via the van Milen fjord into the Storfjorden and finally to the east side of Svalbard in the Barents sea, see Fig. 6.1.

On the cruise there were three different groups, Den Norske Veritas, SINTEF[1], and the University of Bergen[2]. The latter group consisted of oceanographers, meteorologists and remote sensing people that wanted to do measurements both on open water, in polynyas and on ice. The division of time between all different measurements gave two 24h ice stations, one in fast ice in the Freeman strait and one on an ice floe in the Barents sea, positions are marked in Fig. 6.1.

The objective of the cruise for the Nansen centre was to acquire measurements of sea ice properties, like ice surface roughness and salinity, to be used together with the ESA Spring Campaign 2007 where a new SAR was tested out from an aircraft. The sea ice part of this campaign took place during March 2007 around Svalbard. Another objective was to do *in situ* measurements of sea ice thickness together with snow depth and freeboard for Cryovex 2007, the Cryosat II validation experiment.

[1] A research group at the University of Trondheim
[2] Including NERSC

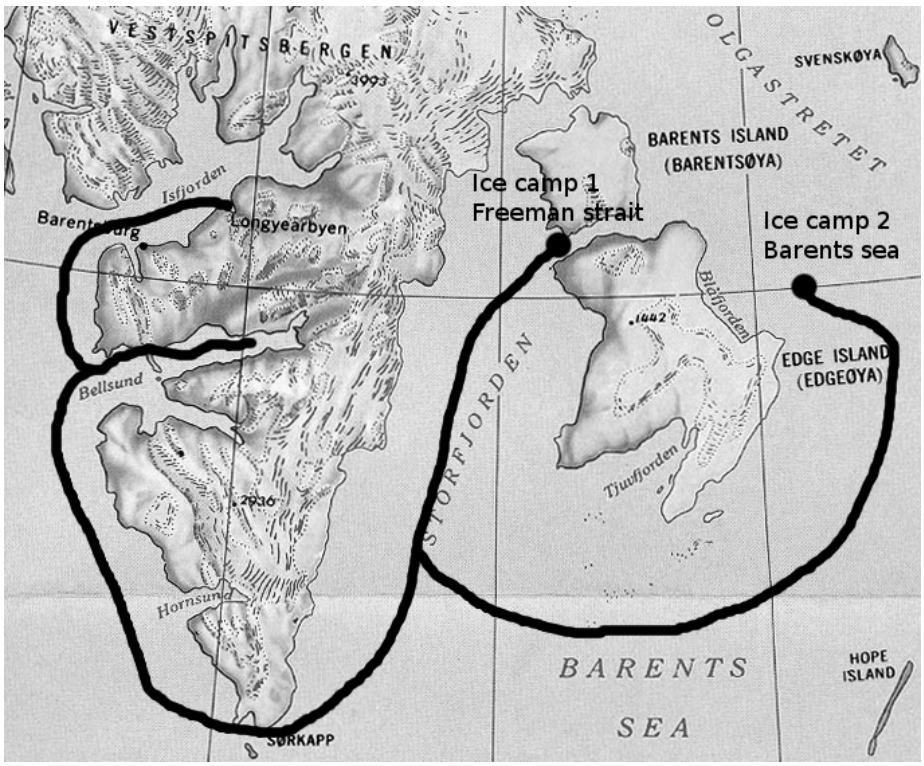

Figure 6.1: The KV Svalbard cruise itinerary with ice stations. Map courtesy of the University of Texas Libraries, The University of Texas at Austin.

6.2 Method and results

6.2.1 Ice stations

Freeman strait

The Freeman strait was full of heavily deformed fast ice. Because some measurements of other groups were dependant of smooth ice, K/V Svalbard parked in an area of level fast ice (darker area in Fig. 6.2) in the mouth of the strait where the ice camp was established. The strait is quite wide, so a snow mobile had to be used to do the transects[3], which unfortunately meant that they could only be made on the level ice. Here no big changes of ice thickness were expected, so a sparse grid of holes were considered to cover the area well. It was decided to drill holes every 200 metres with ice cores and snow profiles taken every kilometre along two 2000 meter transects, one bearing NNE along-strait and the other WNW across-strait (white lines in Fig. 6.2). The WNW transect later had to be shortened because of deformed ice that was encountered in one direction and protected wildlife in the other. In total 19 holes were drilled. Ice cores and snow profiles were taken at four locations, one at camp, two along

[3]Lines along and across the strait on which holes are drilled with even spacing

Figure 6.2: The Freeman strait ice station. The dark tongue is the level ice in which the ice camp (C) was established. Transects were made along the lines S1 and S2.

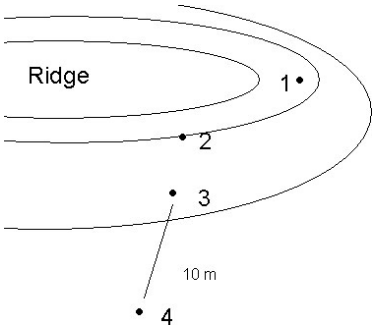

Figure 6.3: Map over the 80 cm high ridge in Freeman strait where four holes were drilled.

NNE section and one in the WNW section. The dominant ice surface roughness on the level ice in Freeman strait was on the scale of mm to cm.

When leaving the ice station K/V Svalbard made an attempt to go through the Freeman strait. The ice here was however too thick, but this gave an opportunity to do measurements in ridged ice. Due to limitations of the ice core drill no cores could be taken for ice thicker than 100 cm, so only measurements of ice and snow thickness and freeboard were made here. The area where the drilling took place was near a ridge about 80 cm high, see Fig. 6.3. Three of the holes, number 1 - 3, where a few metres from each other just next to the ridge while the forth hole was drilled on level ice about 10 metres away from the others. Surface roughness here was in the order of metres.

Barents sea

The Barents sea ice station was located on an ice floe approximately 500 x 800 metres big, 30 km east off the coast of Edgeøya at 78 degrees north, see Fig. 6.1. Two sections were made here, one 400 m long eastward across the floe and one 300 m long southward along the floe, see Fig. 6.4. The southward section started from hole 6 at the eastward section, where the floe was the longest in south direction. Ice thickness on the floe was expected to be more varying than in the strait, so it was decided to drill holes every 20 metres.

In total 33 holes were drilled in the two transects (the black lines in Fig. 6.4) and 4 ice cores were taken at the positions of the black crosses in the same figure. Due to a thin very light snow cover in which density measurements at most places would be impossible to perform, no snow profiles were taken at this station. On the ice floe the dominant surface roughness varied from cm-scale up to half a meter in different areas of the floe. The southern part in general had a rougher surface.

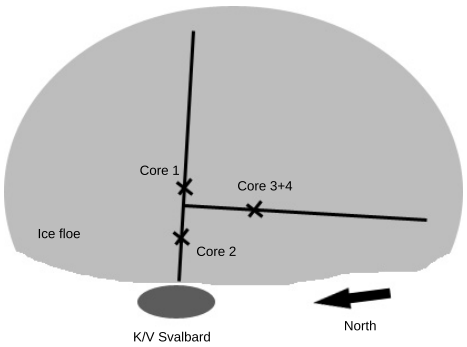

Figure 6.4: Overview of the Barents sea ice station. Transects were made along the black lines and ice cores taken at the crosses. The floe was approximately 500 m wide and 800 m long.

6.2.2 Transects

The holes in the transects were drilled with a 5 cm wide drill. For every hole, ice thickness, snow depth and ice freeboard was measured with a ruler with an accuracy of about 1 cm.

The Freeman sections (Fig. 6.5) were on level ice, about 40-50 cm thick, with only small differences in ice thickness. The only exception is the hole at 1400 m in the WNW section where the measurements were done at the base of a 3m high, probably grounded, ridge. Apart from this particular hole, also the snow cover depth was fairly constant. The ice thickness in the ridge varied a lot as expected, see Fig. 6.7. The thickest measured ice was 750 cm in hole 3 and the thinnest ice was the level ice at hole 4, only 100 cm.

In the Barents sea the ice thickness was much more varying, from less than 20 cm to more than 120 cm. It was also a clear difference between the two sections (Fig. 6.6), the southward section having an average ice cover about 20 cm thicker than the eastern. The snow cover along the south section was also thicker in general.

To estimate ice thickness from sea ice freeboard, the equation for an object floating in equilibrium is used to calculate the theoretical value of ice draft as

$$I_{draft} = \frac{T_s\rho_s + F\rho_i}{\rho_w - \rho_i}, \tag{6.1}$$

with T_s being snow thickness, F being freeboard and $\rho_{s/w/i}$ the density of snow, water and ice respectively. Using the measured freeboard and snow thickness, and the densities proposed by Wadhams [27] of $\rho_w = 1024kg/m^3, \rho_{ice} = 915kg/m^3, \rho_s = 330kg/m^3$, the theoretical ice draft was calculated and plotted together with the measurements from the cross sections in figures 6.5, 6.6, and 6.7.

The average of the measured ice thickness and the theoretical ice thickness[4] of every section was also calculated, the results presented in Table 6.1.

[4]Theoretical ice draft + freeboard

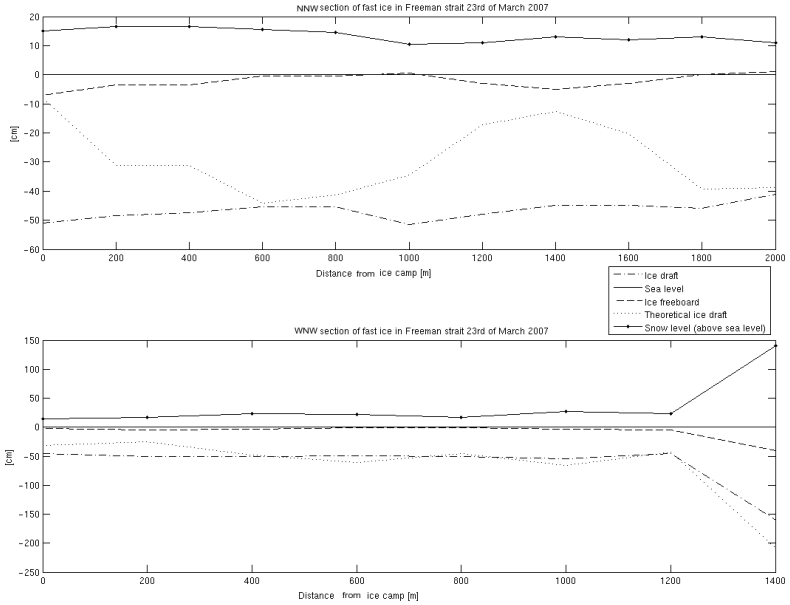

Figure 6.5: The two transects in Freeman strait.

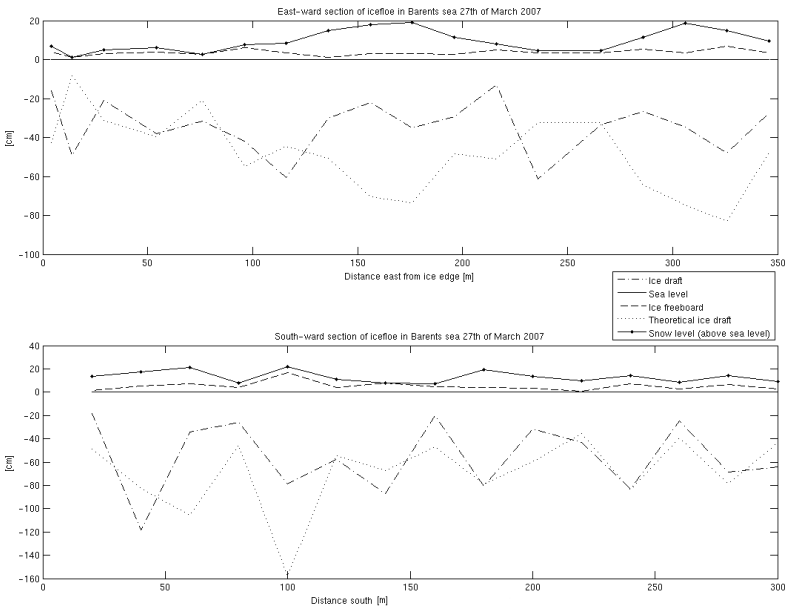

Figure 6.6: The two transects on ice floe in Barents sea.

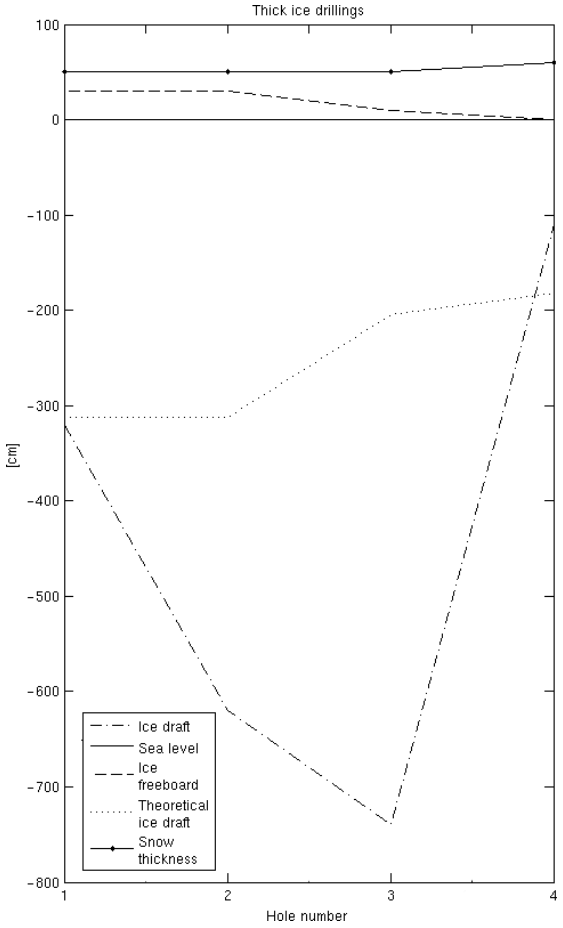

Figure 6.7: The ridge transect in Freeman strait.

Table 6.1: Average measured and theoretical ice thickness.

Ice thickness	Measured [cm]	Theoretical [cm]
Freeman strait		
NNE section	45	27
WNW section	56	59
Ridged ice	465	270
Barents sea		
E section	38	52
S section	61	74

6.2.3 Ice cores and snow profiles

The ice cores were drilled manually pulled out of the ice and put horizontally on the ice before any measurements on them were started. In total eight ice cores were drilled, four in Freeman strait and four in Barents sea. Their lengths are presented in table 6.2.

Table 6.2: Length of the ice cores.

Ice core number	Ice core length	
	In Freeman strait	In Barents sea
Core 1	44	64
Core 2	52	57
Core 3	42	40
Core 4	49	94

Salinity and density

From the ice cores, density and salinity profiles where acquired by sawing the cores into smaller samples[5]. The samples were measured and weighted for density, and then melted for salinity measurements. The conductivity, and hence the salinity, of the melted samples was measured with a Mettler Toledo conductivity sensor. The ice core samples to be melted for salinity measurements were put in plastic boxes, however there were not enough boxes for all samples so some had to go into plastic bags. In the Barents sea some of these bags were leaking and the samples lost.

The Freeman strait salinity curves shows a clear C– shape with the highest salinities found in the upper and lower part of the core, as can be seen in Fig. 6.8. The curves all look similar, except for the high salinity at the top of core 2 and the low salinity at the bottom of core 4.

The Barents sea ice cores do not have the C-shape of the Freeman strait. Here the maximum salinity is found 15-25 cm from the upper surface of the ice to decrease further down, see Fig. 6.9. In core 4 an additional peak in salinity can be found at about 60 cm from the ice surface.

[5]between 5 and 20 cm long

Ice density measurements were only made in Freeman strait, however, problems with knowing the exact volume of an ice core that in many cases fell apart were too big. This gave improbable results, but as qualitative description the ice in Freeman strait was fairly homogenous while it in Barents sea contained one or two layers of slushy ice in all cores but one.

Snow cover

Snow profiles with temperature and density measurements were taken at the same places as the ice cores. Temperature profiles were acquired by digging a pit and measuring the temperature inside the pit-wall for every five centimetres. The temperature of the atmosphere 10 cm above the snow surface was also measured. Snow density was measured by using a snow kit, a piece of snow with known volume was collected and then weighted.

The snow cover in the Freeman strait was in general between 10 and 20 cm hard packed snow which was saturated with sea water up to about 5 cm above the ice surface due to a negative freeboard. The snow density measurements were not made for the entire depth of the snow pack as with the ice density measurements. The measurements therefore only gave a quantitatively result, with a snow density of about 250-300 kg/m^3 at the surface and 400-450 kg/m^3 further down. The flooded snow had a density between 800 and 900 kg/m^3

In the Barents sea the ice floe was covered with a thin layer of snow, between 0 and 20 cm but mostly less than 10 cm. This was cold new snow, so light that taking density samples with any accuracy proved very difficult, therefore no snow density measurements were made. It was however lighter than the snow found in the Freeman strait.

Temperature profiles

The temperature profiles were measured in different ways in the two ice stations. In Freeman strait the core was lifted out of the ice and holes were drilled with even spacing from bottom to top along the core with an electric drill. The temperature was measured in these holes.

In the Barents sea station the temperature was instead measured by drilling a few centimetres into the ice, putting the thermometer-sensor into the hole, measuring the temperature at the current depth, and then drill another couple of centimetres for the next measurement.

In the Freeman strait the air temperature was around -4 ^{o}C at 10 cm above the snow surface. The temperature profiles of all cores and snow profiles are very similar, see Fig. 6.10. A peak minimum is reached about 5 cm below the snow surface, from here the temperature increases evenly to the bottom of the ice sheet where it reaches the freezing temperature of the water.

The temperature profile in the Barents sea, see Fig. 6.11, had an air temperature of was around -8 ^{o}C at 10 cm above the snow surface. Ice core 1 and 2 were taken in areas with very little or no snow so the air-ice boundary was as cold as the air. From here it was a strong gradient the first 10 cm to thereafter stay at almost constant temperature for core 1 and a very small gradient for core

2. Ice core 3 was taken right next to core 4, so the temperature measurements were made in common for both and presented in the core 4 plot in the same figure. There is a temperature gradient down to about 35 cm from where the temperature is almost constant.

6.3 Discussion and conclusions

6.3.1 Sections

The calculations of ice thickness from the known freeboard overestimates the ice thickness in two cases, underestimates it in two and is very close to the actual thickness in one case, as can be seen in Table 6.1. The biggest error is for the short section at the ridge, but here only a few holes were drilled in an area of heavily deformed ice. A much longer section would be needed to give a fair picture of the thickness distribution and average thickness.

In the Freeman strait WNW section a good correlation is present between theoretical ice thickness and measured thickness, in average they just differ a few cm (see Table 6.1). Looking at the lower graph in Fig. 6.5 it can be seen that the curve for the calculated ice draft matches the measured draft well except for the ridge at 1400 m and at 200 m where a high negative freeboard is present. In the NNW section the correlation is not as good, the upper graph in Fig. 6.5 shows that the biggest errors in calculated draft also here comes from holes with a large negative freeboard. One explanation to this could be that ice with negative freeboard is flooded with sea water, hence the snow lying on it will absorb water and become a lot heavier, pressing the ice down even further. A low freeboard is due to either a heavy load or low buoyancy, so calculations with a given load, lower than the true load, and a low freeboard would give a low buoyancy and thus a thin ice cover.

In the Barents sea, the theoretical ice draft of the eastward section Fig. 6.6 matches the measured thickness quite well except for areas with a thick snow cover where calculated ice is much too thick. This implies that the snow density of 330 kg/m^3 used by Wadhams [27] was too high in this case, something that is supported by observations. As mentioned no snow density measurements were made in Barents sea, but the snow here was lighter than any of the snow found in the Freeman strait, where the lowest measured value was 245 kg/m^3. In areas without snow cover, the calculated value is lower than the measured, something that could be because the areas with bare ice were not very large and the surrounding snow could contribute to the load. This was not taken into account in the calculations. For the southward section Fig. 6.6 this relation between snow cover and error in calculated draft is not present. This section however cuts through ice with more rafting and ridging that affects the freeboard more than the snow. This is likely the case for the hole at 60 m. Here the calculated draft is much deeper than the measured draft. This hole was drilled in an area with several small ridges, likely to give buoyancy to the entire area, giving a high freeboard also to thinner ice. The big calculated error at the hole 100 m is probably due to over ice[6] which increased the freeboard without contributing

[6] A layer of ice separated from the main ice sheet by a layer of air

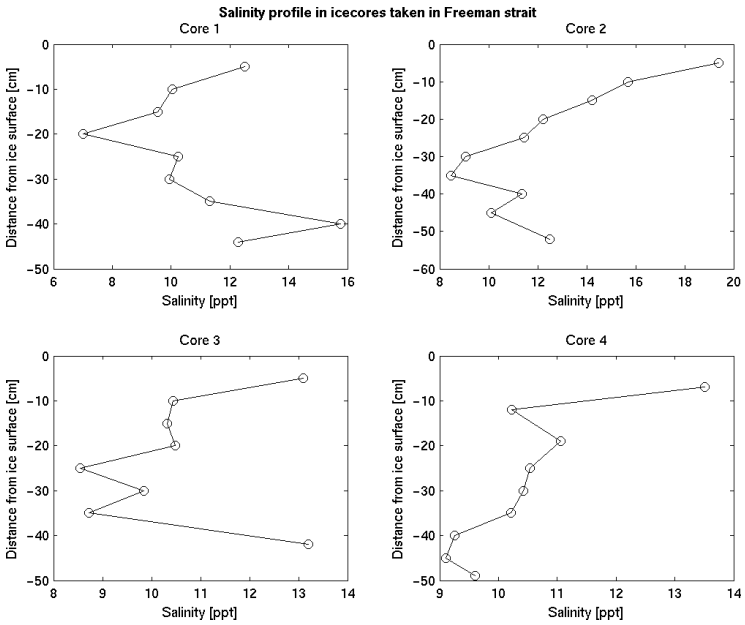

Figure 6.8: Salinity of ice cores in Freeman strait

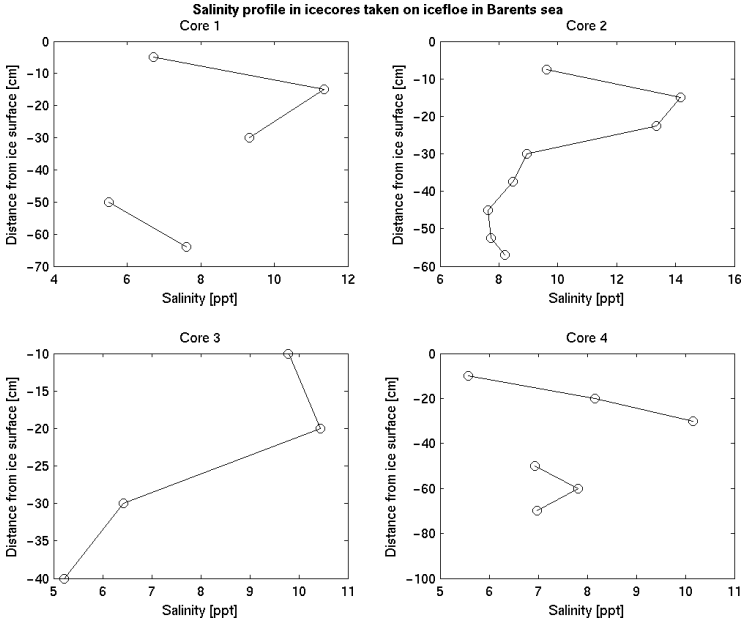

Figure 6.9: Salinity of ice cores in Barents sea

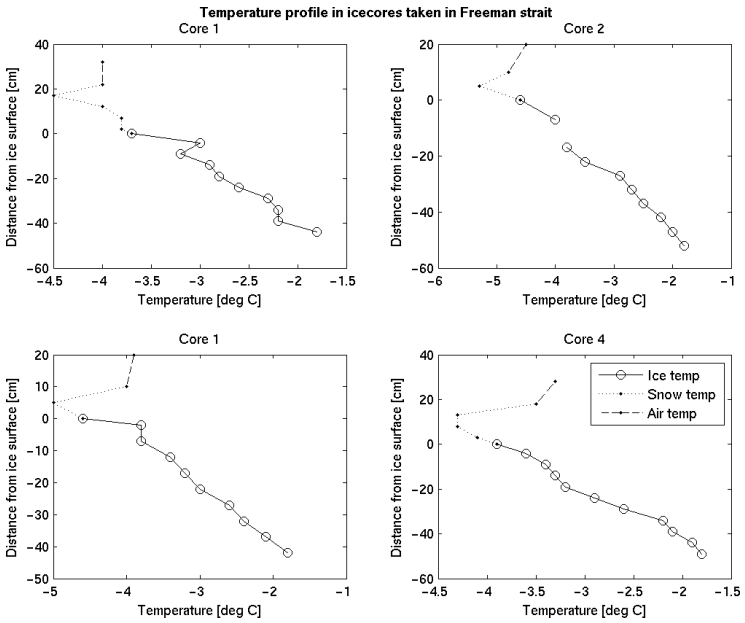

Figure 6.10: Temperature profile of ice and snow in Freeman strait

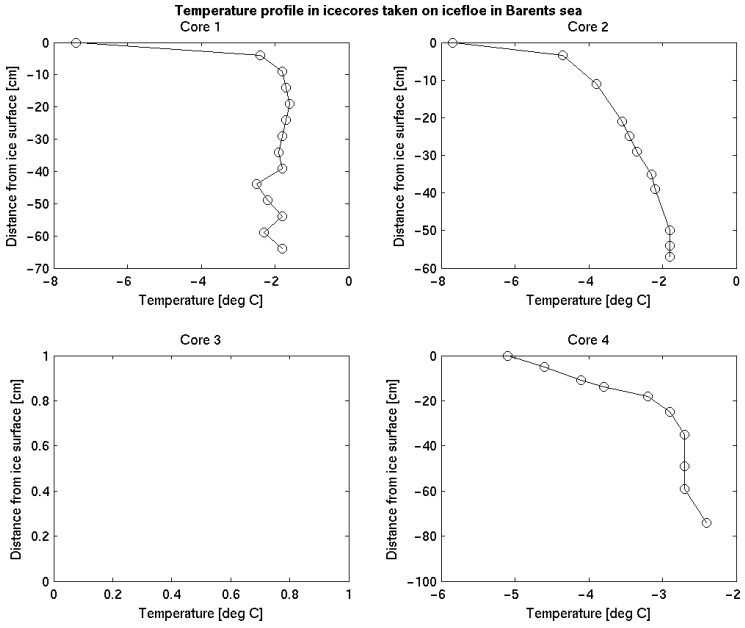

Figure 6.11: Temperature profile of ice cores in Barents sea

with much weight.

6.3.2 Ice cores and snow profiles

From table 6.2 it can be seen that ice core 3 in Barents sea was the shortest of the obtained ice cores, while core 4 was the longest. These cores were taken with only 1 meter in between in an area with rafting. This shows that the ice thickness can vary a lot over small distances. Obviously the 20 m spacing between the holes in the transects will not give the whole picture. An idea for another time is to drill a grid of *e.g.* 10 x 10 m with 1 m hole spacing and measure the thickness, to get an idea of the small scale variability.

Salinity and density

As mentioned the ice density measurements were not reliable. In several cases the ice density was higher than that of the water it was floating on. The problem with measuring ice density was that it was difficult to know the exact volume of the sample that was weighted. From the results the samples, which were measured before sawing, were probably sawed too long and thereby acquiring a larger volume than the one used in the calculations. By using a mitre block and measuring the samples after sawing the reliability for solid ice would increase. However, for soft ice that falls apart when sawing in it another method is needed.

The salinity peak just beneath the surface of the ice cores in Barents sea coincides well with the soft slushy layer that was found in all cores but core 4. This could be a result of flushing, where snow has been flooded with sea water and the upper 10 cm of this saturated snow has later frozen with a resulting loss of salt. This snow-ice could have insulated the rest of the snow slush sufficiently from the cold atmosphere for it not to freeze completely. The absence of old snow on the ice floe speaks for this flooding theory.

A general problem with salinity measurements from ice cores is that when a core is lifted out of the ice, the brine in its bottom part flows out. This results in measuring a lower salinity than the true value in the lower tens of centimetres of the core [12].

Temperature profiles

The temperature profiles in the Freeman strait with their peak minimum about 5 cm down in the snow are likely due to that the air temperature has been colder than at the time of measurements and that the warmer air not yet have had the time to warm up the entire snow cover. The almost constant temperature gradient in the ice sheet implies that the ice is fairly homogenous. It is also either well insulated by the snow cover, so that a shorter cold or warm spell would not affect the temperature further down in the ice, or no larger changes in temperature has taken place recently.

In the Barents sea the method for acquiring the temperature profiles was not optimal. In the upper part of the ice sheet it worked well, but some way down into the ice water started to flow into the hole. It is unsure where this water

came from, if it was percolating up through the ice below or if it was brine from above flowing down. Either way the measurements after the point when water started filling the hole would be affected either from the environment above or below the point where measurements were made. These measurements are in other words not reliable below a certain point, unfortunately this point was not recorded. In the upper part however, a strong temperature gradient is present in all cores, which shows that a recent temperature drop has taken place.

Bibliography

[1] J. Stroeve, M. M. Holland, W. Meier, T. Scambos, and M. Serreze, "Arctic sea ice decline: Faster than forecast," *Geophys. Res. Lett.*, May 2007.

[2] S. S., K. K., and S. M., "Ice drift in the fram strait from envisat asar data." NERSC, 2006.

[3] J. C.R. and A. J. (ed.), *Synthetic Aperture Radar Marine User's Manual*. U.S. Department of commerce, 2004.

[4] J. A. (ed.), "Remote sensing using microwaves." Department of Radio and Space Science, Chalmers University of Technology, 2002. Göteborg, Sweden.

[5] C. J.C. and M. R.N., *Synthetic aperture radar - systems and signal processing*. John Wiley and Sons, Inc, 1991.

[6] E. S. Agency, "Esa earthnet." http://earth.esa.int/, 2007. Online; acessed April 2007.

[7] N. R. Canada, "Canada centre for remote sensing website." `http://ccrs.nrcan.gc.ca/`, August 2007.

[8] L.-M. C. and P. E., "Speckle noise characterization in correlated measurements and its application to synthetic aperture radars," *SPIE*, vol. 6341 63411D-1, 2006.

[9] D. S. and S. A., *Principles and Applications of Imaging Radar, Manual of Remote Sensing*, vol. 2. John Wiley and Sons, Inc, 3 ed., 1998.

[10] L. D. and M. R, *Polar remote sensing, vol.1 Atmosphere and ocean*, vol. 1. Springer- Verlag Berlin and Praxis publishing Ltd, Chichetser, UK, 2006.

[11] C. F. (ed.), *Microwave Remote Sensing of Sea Ice*. American Geophysical Union, Washington, DC, 1992. AGU Monograph No 68).

[12] N. D., *Thermodynamic and Fluid-Dynamical Processes in Sea Ice*. PhD thesis, University of Cambridge, 2005.

[13] J. S. Wettlaufer, M. G. Worster, and H. E. Huppert, "Natural convection during solidification of an alloy from above with application to the evolution of sea ice," *J. Fluid Mech*, no. 344, pp. 291–316, 1997.

[14] M. Finn, *On the properties of sea-ice. Norwegian North Polar expedition with the Maud 1918-1925.* 1927.

[15] W. P., *Ice in the Ocean.* Gordon and Breach Science Publishers, 2000.

[16] M. W. *et al.*, "All about sea ice." `http://nsidc.org/seaice/index.html`, August 2007.

[17] Y. Aksenov, *Local ice cover deformation and mesoscale ice dynamics, part 1 Final scientific report*, ch. Local deformation from field studies. Helsinki University of Technology, Ship Laboratory, 1999.

[18] "International sea ice summer school." Lectures, 2007.

[19] S. S., W. J., S. M., and K. K., "Sea ice drift analysis in the barents sea 2006." NERSC technical report no. 274, 2006.

[20] L. Bertino, "Deputy director, nersc." Personal communication.

[21] B. technologies, "Sar tool." `http://www.boost-technologies.com/web/en/sartool.html`, September 2006.

[22] "Institut franais de recherche pour l'exploitation de la mer." `www.ifremer.fr`, October 2006.

[23] "Argos users manual online." `http://www.cls.fr/manuel/html/sommaire.htm`, July 2007.

[24] "The damocles project." `http://www.damocles-eu.org`, August 2007.

[25] K. R, "Deformation of the arctic ocean sea ice cover between november 1996 and april 2007: A survey," tech. rep., JPL TRS 1992+, 2000.

[26] K. *et al.*, "The ncep/ncar 40-year reanalysis project," *Bull. Amer. Meteor. Soc.*, vol. 77, pp. 437–470, 1996.

[27] W. P. *et al.*, "Relationship between sea ice freeboard and draft in the arctic basin, and implications for ice thickness monitoring," *JGR-Oceans*, vol. 97 No. C12, pp. 20,325–20,334, 1992.